Renewable Energy 255 (2025) 123842

Contents lists available at ScienceDirect

Renewable Energy

journal homepage: www.elsevier.com/locate/renene

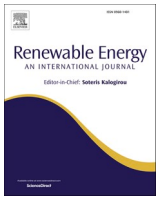

Sound propagation analysis of a 10 MW wind turbine: Influence of the tower, operational states, and atmospheric conditions

Zhenye Sun [a,b], Weijun Zhu [a], Eduardo Jané [b], Xukun Wang [b], Wen Zhong Shen [a], Esteban Ferrer [b,c,*]

[a] School of Electrical Energy and Power Engineering, Yangzhou University, China
[b] ETSIAE-UPM-School of Aeronautics, Universidad Politécnica de Madrid, Madrid, Spain
[c] Centre for Computational Simulation, Universidad Politécnica de Madrid, Madrid, Spain

ARTICLE INFO

Keywords:
Wind turbine
Sound propagation
Actuator line
High-order h/p
Wind turbine wake
Parabolic equations

ABSTRACT

Accurate prediction of wind turbine noise propagation over long distances is critical to mitigate community impact but remains challenging due to complex interactions between wake and atmospheric conditions. This study investigates the sound propagation of a 10 MW wind turbine using a hybrid computational approach that combines high-fidelity flow simulations and parabolic equation (PE) modeling. Large-eddy simulations with actuator lines (for the rotating blade modeling) and immersed boundary methods (for the tower and nacelle modeling) resolve the turbulent wind turbine wake structure, including rotor, tower, and nacelle effects, under rated (11.4 m/s) and near cut-out (24 m/s) wind conditions, with constant inflow and neutral atmosphere boundary layer (ABL) inflows. Noise propagation is analyzed using a wide-angle Parabolic Equation (PE) solver, utilizing as base flow wake generated by the high fidelity large-eddy simulation solver. The methodology allows the study of the acoustic refraction of wind turbine noise under a variety of conditions. We systematically study the effects of the rotor (without tower or nacelle), the full turbine with constant inflow, and the full turbine with a neutral ABL, for rated and cut-out operating conditions. The results demonstrate that wake-induced velocity gradients significantly alter sound propagation paths, with the tower and nacelle introducing asymmetric refraction effects that amplify near-ground noise levels. Atmospheric refraction profiles strongly modulate propagation: upward refraction (e.g., nighttime conditions) create quiet zones, while downward refraction exacerbates noise levels. Under rated condition, the ISO-9613-2 method and the solver PE without wake predict lower sound pressure level (maximum 5 dB) than the PE considering wakes (both with constant inflow and neutral ABL inflow) at critical residential ranges (500–1000 m downstream of the turbine), highlighting the need for advanced models for regulatory compliance. The study underscores the importance of integrating wake and atmospheric effects in noise assessments, providing a framework for optimizing wind farm layouts and mitigating acoustic environmental impact.

1. Introduction

With the large-scale installation of wind turbines near residential areas, addressing long-distance noise propagation has become a growing challenge. Wind turbine noise often travels within the wake of the turbine and when combined with varying meteorological conditions, the propagation process becomes highly complex, making it difficult to accurately model using simple analytical formulas. Consequently, a detailed investigation of the phenomena of acoustic propagation is required. Furthermore, a clear distinction of the effect on sound refraction of the different phenomena altering wind turbine wakes (e.g., the presence of the tower and nacelle in the simulations of acoustics, the atmospheric boundary layer) remains unexplored and is the subject of this work.

Advanced numerical methods such as computational aeroacoustics (CAA) can be used to investigate the mechanisms of flow-induced noise. The most accurate CAA approach is direct numerical simulation (DNS) [1,2], where both fluid flow and sound are calculated directly by solving the compressible Navier-Stokes (NS) equation. However, proper resolution of the entire range of spatial and temporal scales in complex flows

* Corresponding author. ETSIAE-UPM-School of Aeronautics, Universidad Politécnica de Madrid, Madrid, Spain.
E-mail address: esteban.ferrer@upm.es (E. Ferrer).

https://doi.org/10.1016/j.renene.2025.123842
Received 20 February 2025; Received in revised form 17 June 2025; Accepted 21 June 2025
Available online 27 June 2025
0960-1481/© 2025 The Authors. Published by Elsevier Ltd. This is an open access article under the CC BY-NC-ND license (http://creativecommons.org/licenses/by-nc-nd/4.0/).

using DNS requires a great deal of computational resources. Consequently, conventional CAA methods are neither efficient in modeling the noise sources of wind turbines nor in predicting noise propagation in large domains. To alleviate the computational burden of these types of models, Hardin and Pope developed the flow/acoustic splitting method in 1994 [3]. Shen and Sørensen [4–6] investigated a modified splitting method for near-field acoustic simulations of flows past a cylinder and an airfoil, encompassing both laminar and turbulent regimes. Employing second-order finite volume/finite difference methods for fluid dynamics and acoustic computations, their studies yielded promising results, thereby confirming the efficacy and practicality of the splitting method for low-Mach number acoustic simulations. Based on the work of Shen and Sørensen, Zhu [7] incorporated high-order finite difference schemes to solve the acoustic perturbation equation with 4th to 12th order accuracy, while the flow field is resolved using a second-order finite volume incompressible solver. At each time step, the incompressible flow variables serve as input to the inviscid acoustic equation. This method has been successfully applied to simulate airfoil noise generation, proving good agreement with the experimental noise spectra. Although the above splitting method reduces the computational cost compared to CAA/DNS, its cost is still unaffordable in most wind energy engineering applications. Typically, noise generation and noise propagation are computed separately to further reduce computational costs, following acoustic analogies. Therefore, the level of sound pressure at a given reception point is related to the sound power at the source and the propagation losses of the noise through the complex wake field. To obtain the sound power level of a wind turbine source, the engineering model [8] can be used, which combines Blade Element Momentum (BEM) calculations [9,10] and a semi-engineering BPM model [11]. Under this approach, the sound power level of a wind turbine depends on the rotor shape and its operating conditions, such as its rotational speed, the inflow wind speed profile, turbulence level, air density, and viscosity, etc. This paper focuses on noise propagation.

There are several outdoor sound propagation modeling techniques, as reviewed by Berengier et al. [12]. The propagation of sounds can be investigated using analytical, numerical, and experimental methods. Computationally, the ISO-9613-2 method is the cheapest, but shows large deviations with respect to the measured noise levels of the wind turbines [13]. Numerical techniques, including the Fast Field Program (FFP) [14] and Boundary Element Methods (BEM) [15,16], have been successfully validated for a variety of typical scenarios. The numerical approaches described above may not be suitable when the propagation medium is non-stationary, showing range-dependent velocity fluctuations. For example, the FFP method is inherently limited to systems with a layered atmosphere and a homogeneous ground surface. Therefore, range-dependent sound speed profiles or ground impedances cannot be accurately modelled by the FFP method, which means that the FFP cannot consider the effects of wake on noise propagation.

Two years of continuous sound measurements [13] were conducted at two wind turbine sites in Sweden to investigate the impact of varying meteorological conditions. Vertical profiles of wind speed, direction, temperature, and relative humidity were measured along with sound levels, revealing substantial variations in wind turbine sound propagation due to atmospheric refraction. Indeed, meteorological effects on sound propagation become increasingly significant with distance, being most noticeable at distances ranging from 400 to 1000 m from the turbines. Therefore, for far-field predictions under complex atmosphere conditions, models such as the Parabolic equation (PE) method [17,18] are usually selected, balancing numerical accuracy with computational efficiency. According to an estimation of low frequency and infrasound noise from wind turbines at 1238 residences within Canada, field measurements detected spectral peaks extending up to 10 km from turbines, covering frequencies from 0.5 to 70 Hz. These measurements, integrated with meteorological data on site, aligned with the predictions of the PE simulations [19]. The PE equation is simplified from the wave equation which describes the behavior of sound waves. This involves mathematical manipulations that exploit the assumption of predominantly forward propagation. The PE method is not limited to a layered atmosphere and a homogeneous surface of the ground. There are different versions of the PE method, like the Crank-Nicholson Parabolic equation (CNPE, introduced by Gilbert and White in 1989) [20,21] method, and the Green's Function Parabolic equation (GFPE, developed by Gilbert and Di [22]).

In this work, a 2D (two-dimensional) PE method of wide-angle CNPE is used to simulate the phenomenon of noise propagation. The parabolic equation is solved numerically using techniques like a finite difference method, which involves dividing the propagation space into a grid and iteratively calculating the sound pressure level at each grid point. Each PE simulation yields a steady-state solution for a specific frequency. To simulate sound propagation from wind turbines to receivers in an inhomogeneous moving flow, the effective speed of sound approach is adopted, which requires inputs of the flow field covering the source and receivers. The flow field surrounding the wind turbines can be obtained via wake models, wake measurements, or computational fluid dynamics (CFD) simulations. There are some studies that use the wide-angle CNPE to investigate the influences of atmospheric conditions on the propagation of wind turbine noise, but do not consider the effects of wind turbine wake [23–26]. In 2011, wind turbine wake effects on noise propagation were first studied [27] by the team led by D. Heimann at DLR in Germany, where a three-dimensional ray-based sound particle model was used [28]. This method has been compared to other models for wind turbine noise analysis and has been cost-effective compared to 3D (three-dimensional) models. Numerous works cover this topic. For example, reference [29] focuses on the impact of diurnal variability on the propagation of wind turbine noise. Barlas et al. used the wide-angle CNPE method to study the effects of wake and atmospheric conditions on wind turbine noise propagation [30–32], clearly showing their influence. More recently, Colas et al. conducted detailed work on wind turbine noise propagation in the wake of rotors and hills [33,34]. They developed a solver based on the linearized Euler equations (LEE), which combines a flow model based on LES and an extended source model based on Amiet's theory. They compared the LEE method with the state-of-the-art PE methods. Among the PE methods, they considered the wide-angle vector PE, which is limited to flat terrain ($WAPE_{vec}$), as it can consider all velocity components (but only uses the horizontal one). The better option is the wide-angle PE with an effective sound speed approximation and the ability to consider a 3D topography (WAPEtopo). The LEE and WAPEvec methods perform almost identically in flat and hilltop topographies. The $WAPE_{topo}$ method introduces phase errors that are attributed to the effective sound speed approach and the steep hill slope. Nevertheless, its rotation-averaged SPL and amplitude modulation (AM) are close to the LEE method. The main weakness of this LEE method is the high computational cost. A recent study [35] using 3D PE simulations to analyze low-frequency rotor wake effects demonstrates that these three-dimensional wake phenomena markedly alter sound propagation. Consequently, 2D PE models may underestimate the resulting SPL. The above studies have made solid contributions to the topic of wind turbine noise propagation, which sheds light on this study on aspects such as how to deal with the noise source and how to choose the correct method. In this work we will use a wide-angle PE solver.

In what follows, we address the gaps in knowledge regarding noise propagation, specifically by studying and quantifying:

- Contributions of the rotor, nacelle and tower wake to the propagation of wind turbine noise.
- Impact of different atmospheric conditions on the propagation of noise.
- Comparison of rated vs. cut-out conditions to assess their influence on sound propagation.

This paper is organized as follows: In Section 2, the CFD solver simulates flow fields and wakes and the noise propagation model are

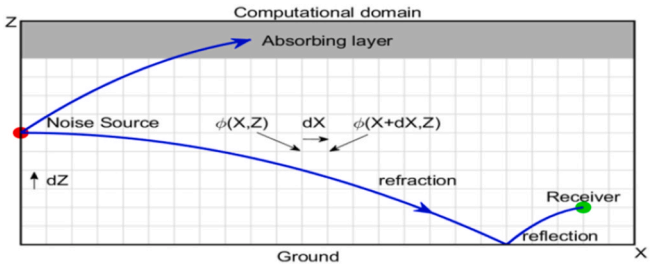

Fig. 1. Demonstration of the simulation domain for the parabolic equation solver.

described. Then, Section 3 provides results for the flow field, noise source, and detailed results of noise propagation under different wind turbine wakes, atmosphere conditions, and operating conditions (rated vs cut-out). Finally, the conclusions are presented in Section 4. Appendices A and B provide details of the CFD simulations and ABL generation.

2. Numerical methodology

The proposed methodology considers flow fields obtained from CFD simulations. These flow fields are then used to propagate the acoustic sources of wind turbines over long distances using a propagation wave equation solver.

2.1. Flow simulations

Flow simulations have been performed using Horses3D, a high-order spectral element CFD solver [36], which is open source and available on Github (https://github.com/loganoz/Horses3D). It is developed at ETSIAE-UPM (the School of Aeronautics at the Polytechnic University of Madrid). Horses3D is a 3D parallel code designed to simulate fluid flow phenomena and employs a high-order discontinuous Galerkin spectral element method (DGSEM) implemented in modern Fortran 2003. The solver efficiently handles simulations governed by both compressible and incompressible Navier-Stokes equations. Horses3D is equipped to manage body-fitted, immersed boundaries (IB), and actuator lines. Here, we select the actuator line method (ALM) to simulate the rotating blades and resulting wakes. The ALM models the turbine blades as lines of distributed forces, which are obtained from tabulated airfoil polars. The resulting rotating lines mimic rotating blades and provide accurate flow fields and wakes at a computationally affordable cost [37]. To include the nacelle and the tower, we use the immersed boundary method (IBM), which explicitly includes the three-dimensional shape of the object [36–38].

The distributed forces of the ALM and the IBM forcings are inserted into the NS momentum conservation equation as source terms:

$$\boldsymbol{U}_t + \nabla \bullet (\boldsymbol{F}_{iv} - \boldsymbol{F}_{v+t}) = \boldsymbol{S}(\boldsymbol{U}), \tag{1}$$

where $\boldsymbol{U}_t$ is the state vector of conservative variables, $\boldsymbol{F}_{iv}$ is the inviscid fluxes, $\boldsymbol{F}_{v+t}$ is the viscous and turbulent fluxes and $\boldsymbol{S}(\boldsymbol{U})$ is the source term. However, the mass and energy conservation equations, on the other hand, remain unchanged. The aerodynamic forces in the blades are calculated using the blade element theory knowing the aerodynamic properties of airfoils at each section of the discretized blade and the characteristics of the resolved flow field. To avoid numerical instability, the aerodynamic forces are smeared using 3D Gaussian regularization to get the source term force to be exerted in each point of the high-order computational mesh [37].

$$\eta_\epsilon(d) = \frac{1}{\epsilon^3 \pi^{\frac{3}{2}}} e^{-(d/\epsilon)^2}, \tag{2}$$

where d is the distance between an actuator point and an arbitrary node. The aerodynamic forces are updated using the newly computed velocity field after each iteration, and then the source term forces S(Ut) are accordingly recomputed in the next iteration. This combined DGSEM and ALM method provides a balance between computational efficiency and accuracy, making it a powerful tool for simulating wind turbine flows and obtaining input for sound propagation simulations, as described below. In the simulations, the compressible NS equations (with a low Mach number of 0.1) are solved using the large eddy simulation (LES) model of Vreman [39]. To advance the solution in time, an explicit Runge-Kutta 3-time marching scheme is used (with $CFL<0.5$ in all cases).

2.2. Noise propagation using parabolic equations

The sound propagation wave equation is solved in a spatial domain, as shown in Fig. 1, for each frequency. For wind turbine fields, the flow is treated as incompressible. The 3D Helmholtz equation can be reduced to the 2D Helmholtz equation by the axisymmetric approximation in a moving atmosphere [17].

$$\left[\frac{\partial^2}{\partial X^2} + \frac{\partial^2}{\partial Z^2} + k_0^2(1+\varepsilon)\right] Q_c^2 = 0, \tag{3}$$

where $Q_c = P_c X^{1/2}$, P_c is the complex pressure amplitude, k_0 is the reference wave number, c_0 is the reference sound speed 340 m/s, $\varepsilon=(c_0/c_{eff})^2 - 1$, c_{eff} is the effective sound speed. In the PE method the receiver is located at $X > 0$, and we consider only waves traveling in the positive X direction; back scattering is neglected. Eq. (3) reduces to the one-way wave equation. If we express Q_c by the envelope of the pressure

$$Q_c(X,Z) = \phi(X,Z)\exp(ik_0X), \tag{4}$$

The one-way wave equation is obtained

$$\frac{\partial \phi}{\partial X} = ik_0(Q-1)\phi, \tag{5}$$

here we use the Padé (1,1) approximant of the operator Q

$$Q = \frac{\frac{1}{2}\left(\varepsilon + \frac{1}{k_0^2}\frac{\partial^2 \phi}{\partial^2 Z}\right)}{1 + \frac{1}{4}\left(\varepsilon + \frac{1}{k_0^2}\frac{\partial^2}{\partial^2 Z}\right)}, \tag{6}$$

These equations are solved via finite differences with a Crank-Nicolson scheme. The resulting solver is usually called 2D PE solver of wide-angle Crank-Nicholson type (WAPE). Detailed derivations of the equations can be found in Ref. [29]. The WAPE method above will be used in this study and propagation phenomena, such as refraction, will be caused by the variation of ε. The flow velocity components, which lead to the variation of ε, may come from field measurements, empirical expressions, or numerical simulations (used in this paper). The effective sound speed approximation is widely used in PE methods. Recently, an extra-wide-angle parabolic equation (EWAPE) has been introduced that does not rely on the effective sound speed approximation [40].

As mentioned above, here we use the WAPE method, which is based on a one-way wave equation. The noise source is configured on the left boundary (where $X = 0$) with a starting function $\phi(0, Z)$, which is a classical approach required to represent a monopole source [17,18]. This starting function is then extrapolated stepwise towards the positive X direction to obtain $\phi(0 + dX, Z)$. After iterating towards the right boundary, the whole field of complex pressure amplitude $\phi(X, Z)$ is computed. The horizontal simulation range is determined by the receiver's location. However, the size of the vertical domain is flexible, such that the height of the domain can vary with the simulated frequency, because at least eight grid points are needed to represent a sound wave. The boundary condition applied on the surface of the ground is controlled by the impedance of the ground. In this study, the empirical model for the normalized impedance Z_m of absorbing

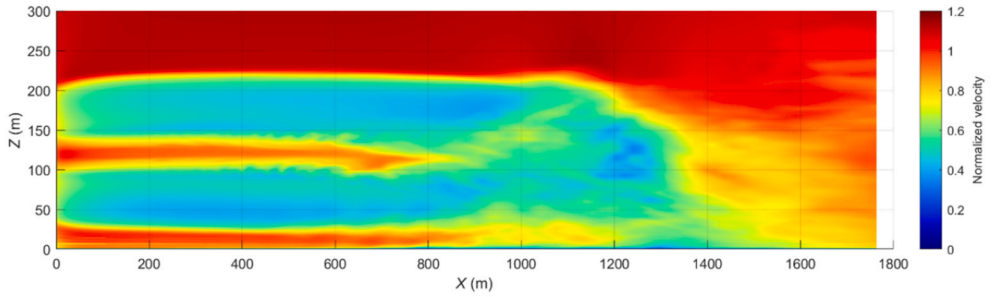

(a) Rotor-rated: Average flow field under V_{in} = 11.4 m/s (no tower and nacelle)

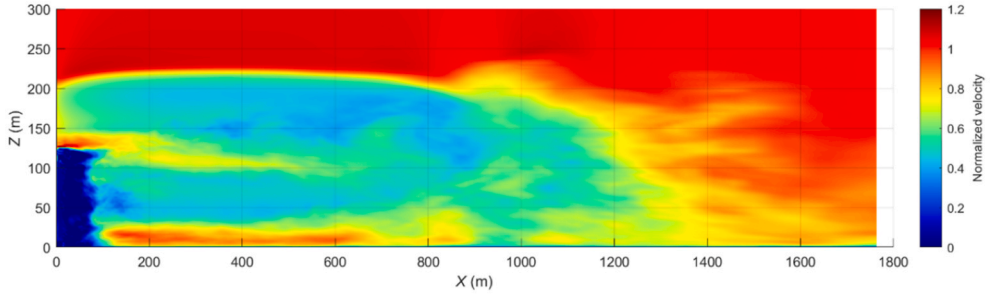

(b) Turbine-rated: Average flow field under V_{in} = 11.4 m/s

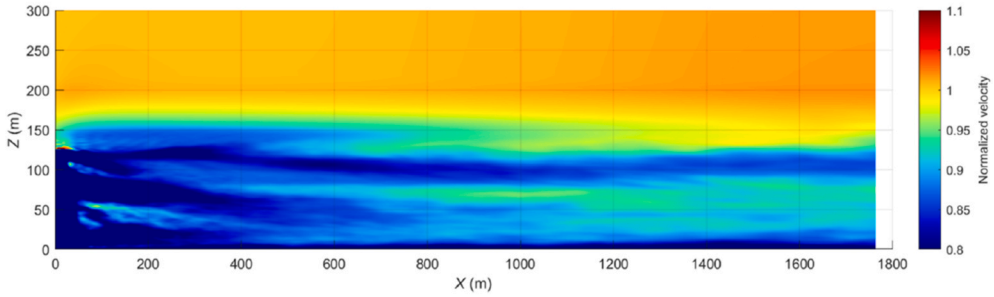

(c) Turbine-Cutout: Average flow field under V_{in} = 24 m/s

Fig. 2. Horizontal velocity component downstream of the wind turbine from the CFD simulation, with constant inflow as the inlet boundary.

materials developed by Delany and Bazely [41] is used, which is only related to two parameters. They are the flow resistivity σ and the frequency. The boundary condition applied to the top surface is constant $Z_m = 1$, so that the vertical sound wave through the top surface vanishes without reflection. However, other waves are partially reflected into the simulation domain. To sufficiently eliminate wave reflections, an absorbing layer with a height of 50 times the wavelength is defined below the top surface, as shown in Fig. 1 by the gray region near the top surface of domain. The height of the absorbing layer increases with decreasing frequency. Detailed mathematical manipulations of the equations can be found in Refs. [17,18].

Integration of the sound intensity over a closed surface surrounding the wind turbine is called the sound power level *SPWL(f)*, which is a quantification of the noise source level of a wind turbine and is the initial condition for calculating the propagation of long-path noise. The *SPL(f)* sound pressure level at the receiver is

$$SPL(f) = SPWL\ (f) - 10\log_{10}(4\pi D^2) - \alpha(f)D + \Delta L, \tag{7}$$

The first term *SPWL(f)* on the right-hand side is the sound power level, which can be obtained by using a combination of the BPM and BEM methods. This methodology considers the contribution from all the blade elements and all the noise mechanisms, such as turbulent boundary trailing edge noise, separation noise, trailing edge bluntness noise, turbulent inflow noise, etc. For brevity, this model is not described in detail, and the reader is referred to Ref. [8]. The second term on the right-hand side of Eq. (7) accounts for the loss of sound pressure due to the spherical spreading of sound waves from a point source, which is normally called geometric attenuation. The third term is called air absorption, which is the multiplication of the absorption coefficient $\alpha(f)$ and the distance D between the source and the receiver. The term $\alpha(f)D$ is negligible for the short distance D and cannot be neglected when D is on the order of a hundred meters, especially at high frequencies. The coefficient $\alpha(f)$ depends on sound frequency, air temperature, pressure, and humidity. The fourth term ΔL (or RSPLD henceforth) is key and accounts for the relative difference in sound pressure level (abbreviated as RSPLD) caused by reflection and absorption on the ground, atmospheric refraction, wind and turbulence, sound barriers, etc. It should be noted that the second and third terms are only related to the absorption coefficient $\alpha(f)$ and the distance D. However, the fourth term ΔL, which will be thoroughly studied in this work, has a relationship with sound reflection and refraction, etc. As a result, the fourth term ΔL is different in nature from the second and third terms, and its variation along the propagation distance D does not follow a simple linear or logarithmic pattern, which requires the use of numerical methods for its solution and is the focus of this article.

3. Results and discussions

In what follows, we try to systematically separate various physical

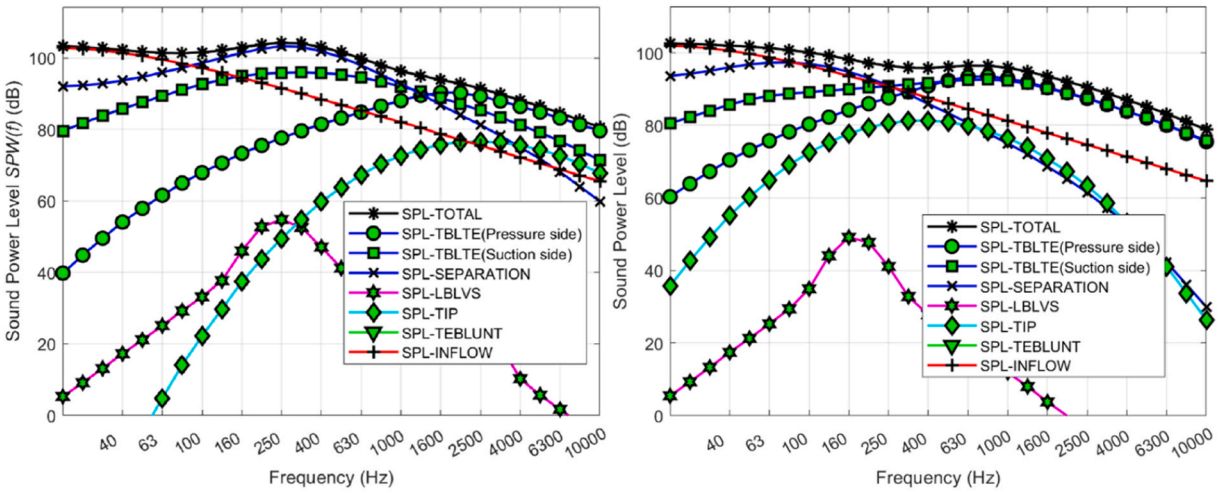

Fig. 3. The sound power level of the DTU-10-MW wind turbine.

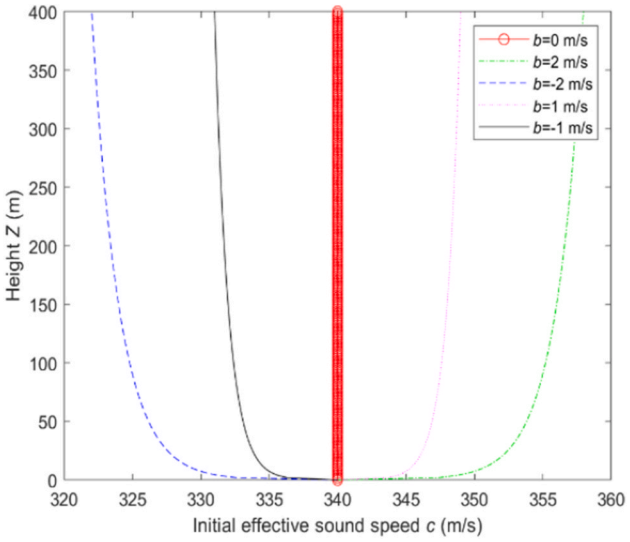

Fig. 4. Initial effective sound speed c (m/s) profile vs height Z (m).

phenomena affecting wake development and noise propagation. Different CFD results are input to the PE solver. One situation is CFD with constant inflow velocity such that the wake contains only turbulence generated by the tower nacelle and rotor. Additionally, we include CFD simulations of only the rotor (no tower or nacelle) to discern the effect of the tower and nacelle on noise propagation. Finally, we include a neutral ABL to understand the modification of atmospheric turbulence in wake shaping and noise propagation. Details on the simulations for ABLs can be found in Appendix A. The physics considered here and influencing noise propagation are:

- Contributions of the rotor, nacelle, and tower.
- Impact of different atmospheric conditions.
- Comparison of wind conditions in rated versus cutout conditions.

3.1. *Preliminaries: flow fields and sound sources*

Throughout this work, the DTU 10-MW Reference Wind Turbine (RWT) [42] is selected, as a representative large wind turbine for onshore and offshore applications. This turbine has a rotor radius of $R = 89.15$ m and a hub height of $Z_{hub} = 119$ m. Examples of the flow fields used for noise propagation are depicted in Fig. 2. The rotor speed is 9.6 RPM in all cases.

Fig. 2(a) shows the averaged CFD flow field after the wind turbine rotor (no tower or nacelle), when using a constant velocity profile $V_{in} = 11.4$ m/s (rated wind speed) as input for the inlet boundary. We name this case 'Rotor-Rated'. Shown in Fig. 2(b) is also the averaged flow field for the rated wind speed, but the difference from Fig. 2(a) is that the whole wind turbine including the rotor, tower and nacelle is simulated in CFD. We name this case as '*Turbine-Rated*'. Shown in Fig. 2(c) is the case '*Turbine-Cutout*', where CFD is run with constant inflow $V_{in} = 24$ m/s (near cutout wind speed, with pitch angle increased to 22.27 deg).

The noise source spectrum *SPWL(f)* for the 10-MW DTU wind turbine, obtained by the Brooks, Pope and Marcolini (BMP) method, is shown in Fig. 3, for the rated and cut-out conditions. The distinct contributions to *SPWL(f)* include turbulent boundary layer trailing edge noise (TBLTE, including contributions from the pressure side and suction side of airfoil surfaces), separation noise, laminar boundary layer vortex shedding noise (LBLVS), tip noise, trailing edge bluntness noise (TEBLUNT), and inflow noise. There are notable differences in trailing edge noise that affect the overall spectra. In the rated case, the maximum SPWL can be found for a frequency of $f = 315$ Hz, while for cut-out conditions, the maximum is found at lower frequencies near $f = 30$ Hz, which is related to the change in the angle of attachment along the blades. The tow spectra will be used to feed the propagation solver, and the resulting propagations will be analyzed later.

To capture thermal effects on wind-turbine noise, one can either perform costly ABL-resolved CFD under neutral, stable or convective stratification—and then compute acoustics in the resulting wakes—or adopt a "decoupled" strategy, using a neutral-ABL flow field and embedding temperature only via a height-dependent sound speed in a parabolic-equation solver. Full stratified CFD is the most physically complete, since it naturally includes buoyancy-driven changes in shear, turbulence and wake recovery. However, numerous studies have shown that the decoupled method delivers accurate, computationally efficient predictions: Lee etc. [23] demonstrated that this decoupled method, when supplied with a neutral wake profile and an effective sound speed, can predict far-field noise levels within a few decibels of more comprehensive models. Colas et al. [33] compared a linearized Euler solver to several parabolic-equation formulations and found that PE methods—with temperature entering solely via sound-speed gradients—reproduce broadband noise predictions over both flat and

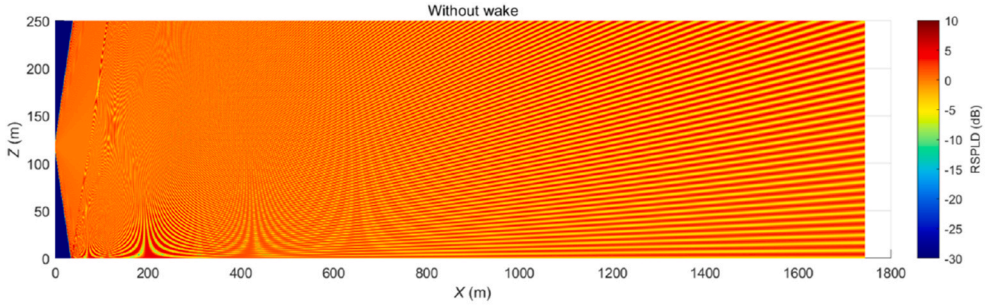

(a) CaseA: without wake, homogeneous atmosphere b=0 m/s

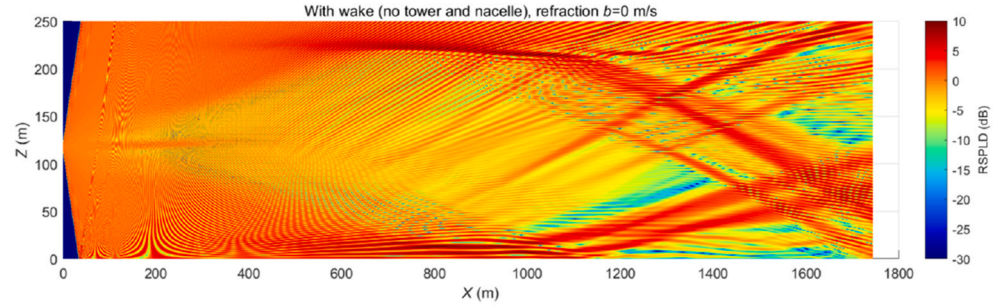

(b) CaseB: with rotor-only wake, homogeneous atmosphere b=0 m/s

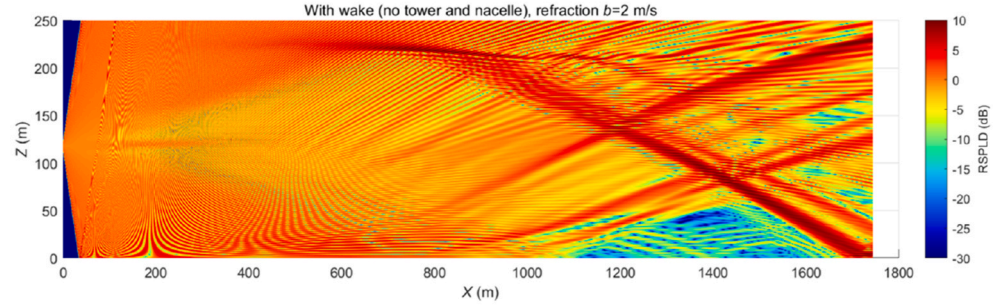

(c) CaseC: with rotor-only wake, downward refraction atmosphere b=2 m/s

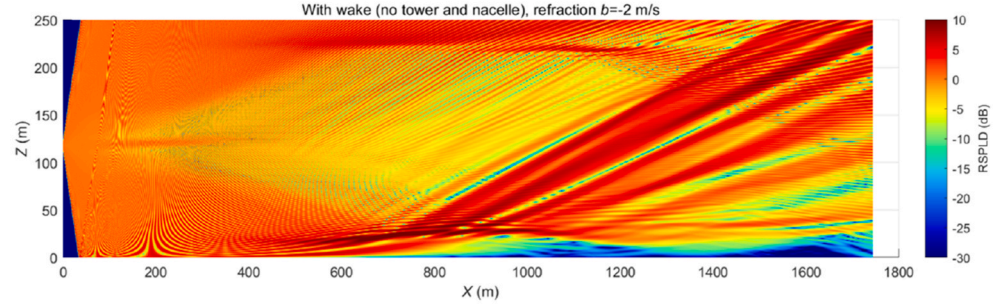

(d) CaseD: with rotor-only wake, upward refraction atmosphere b=-2 m/s

Fig. 5. The contour of RSPLD calculated by PE simulations at $f = 315$ Hz.

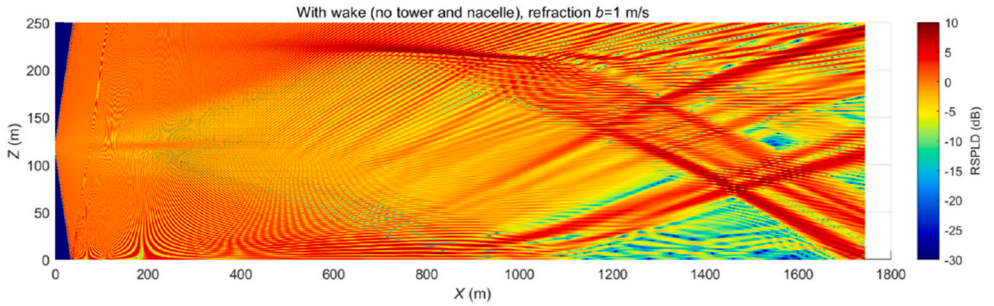

(e) CaseE: with rotor-only wake, downward refraction atmosphere b=1 m/s

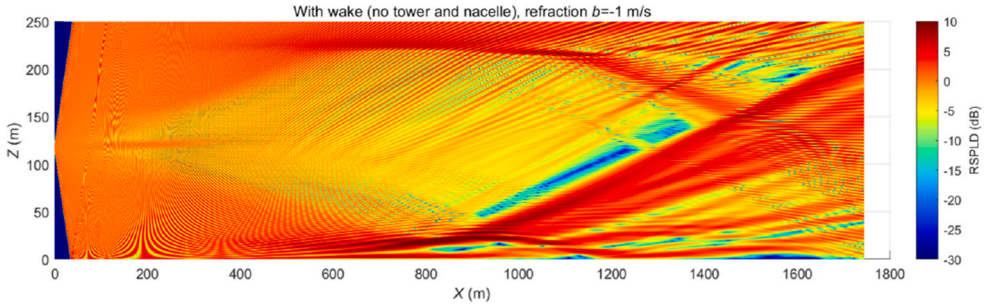

(f) CaseF: with rotor-only wake, upward refraction atmosphere b=-1 m/s

Fig. 5. (*continued*).

Table 1
Six different approximate atmospheric conditions for sound propagation.

Case Name	Atmosphere Condition	Considering Wake
CaseA	Homogeneous, with $b = 0$ m/s	No.
CaseB	Homogeneous with $b = 0$ m/s	wind turbine wake
CaseC	Strong downward refraction, with $b = 2$ m/s	wind turbine wake
CaseD	Strong upward refraction, with $b = -2$ m/s	wind turbine wake
CaseE	Weak Downward Refraction, with $b = 1$ m/s	wind turbine wake
CaseF	Weak upward refraction, with $b = -1$ m/s	wind turbine wake

complex terrain almost identically to the Euler approach. Nyborg et al. [43] further showed, through an inter-model comparison of PE techniques, that wind and temperature effects can be efficiently captured by simply adjusting the sound-speed profile, with inter-method discrepancies generally under 2 dB. Meanwhile, Evans & Cooper [44] highlighted how different meteorological conditions (neutral, stable, convective) influence measured noise levels, underscoring that a neutral-flow assumption may miss extreme refraction effects under strong stratification. In practice, then, full stratified CFD is essential for high-precision or extreme-case studies, while the decoupled neutral-flow plus temperature-dependent sound speed approach offers a fast, and qualitatively reliable approximation for most applications.

Under the above simplified assumptions, the possible upward and downward refraction atmosphere is approximated by setting the vertical distribution of the initial effective sound speed $c_{ini}(z)$ using Eq. (8). The reason why we use Eq. (8) is as follows. The difference between $c_{ini}(z)$ and the reference sound speed c_0 (340 m/s in this paper) contains two initial parts. The first part is caused by the variation of the horizontal velocity v1(z) with height at the left boundary, which represents the

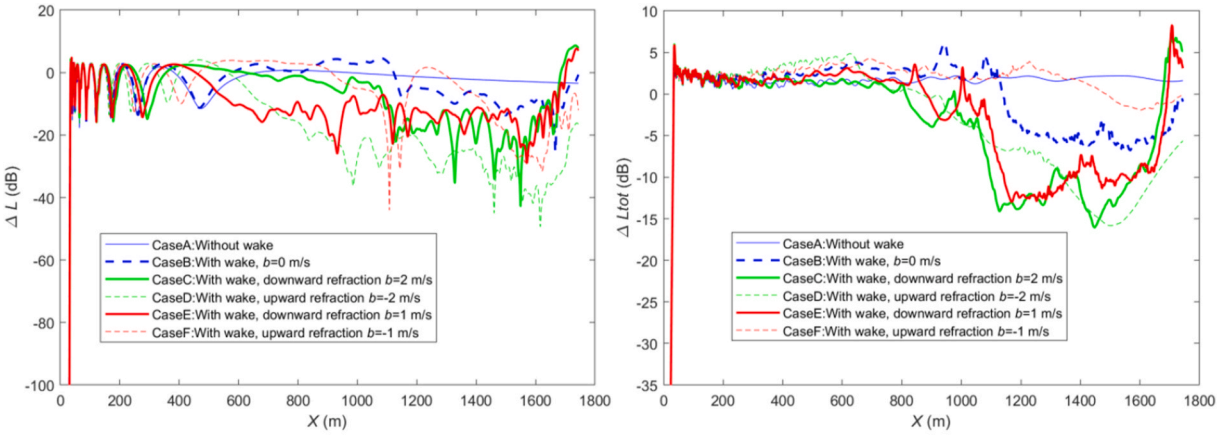

(a) Single frequency f = 315 Hz (b) Averaged over multi frequencies

Fig. 6. The distribution of RSPLD along a horizontal line $Z = 2$ m.

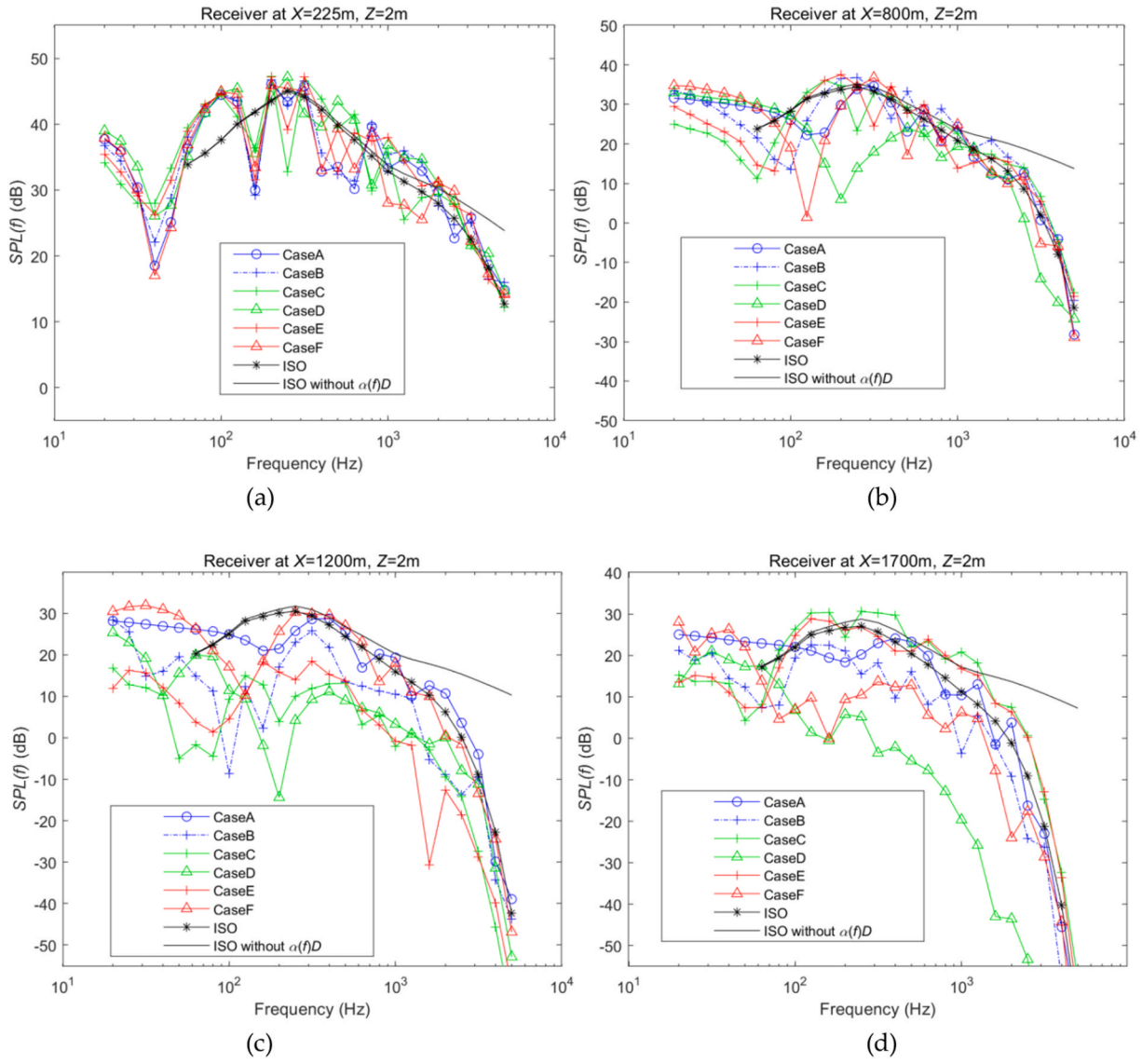

Fig. 7. Sound pressure level spectrum at four receivers at height $Z = 2$ m: (a) receiver at $X = 225$m; (b) $X = 800$m; (c) $X = 1200$m; (d) $X = 1700$m.

CFD inlet boundary under the atmosphere boundary layer (ABL). As a constant profile is used at the CFD inlet boundary, the proper vertical distribution of v1(z) at the inlet is different from reality. The normal distribution of the distribution of $v_1(z)$ under different ABL conditions can be referred to work [45], which is approximated here by the term ln $(Z/Z_0 + 1)$. Therefore, ln $(Z/Z_0 + 1)$ accounts for the effects of the ABL inlet boundary on $c_{ini}(z)$. The second part is caused by the vertical temperature profile, which can also be treated as proportional to ln $(Z/Z_0 + 1)$. As a result, both the ABL inlet boundary and the temperature profile are considered in the initial effective sound speed following the initiation of the acoustic force.

$$c_{ini}(z) = c_0 + b \ln (Z / Z_0 + 1), \tag{8}$$

In the rest of this paper, the reference sound speed $c_0 = 340$ m/s, the roughness height $Z_0 = 0.05$ m and the shape factor of the sound speed profile $b = 0, 2, -2, 1, -1$ m/s will be used. It should be mentioned that the initial effective sound speed c_{ini}, is different with the effective sound speed c_{eff} that will be used in the whole PE domain. To obtain the effective sound speed c_{eff} distribution inside the 2D PE domain, the horizontal velocity in the 2D CFD flow field will be added to c_{ini}. In other words, within the computational domain, c_{eff} is the summation of c_{ini} and the flow speed from the CFD simulation. As shown in Fig. 4, the five initial effective sound profiles represent a homogeneous atmosphere (b = 0 m/s), a heavy downward refraction atmosphere ($b = 2$ m/s), a heavy upward refraction ($b = -2$ m/s), a slight downward refraction atmosphere ($b = 1$ m/s) and a slight upward refraction ($b = -1$ m/s).). The strong refraction atmosphere with $b = 2$ m/s and $b = -2$ m/s may be rare in the real world but are included to present a wider range of possible sound propagation scenarios.

3.2. Wind turbine noise propagation at rated wind speed

As shown in Fig. 1, the noise sources are concentrated in a point located on the left boundary $X = 0$ m, and at hub height $Z = Z_{hub} = 119$ m. According to the noise source spectrum illustrated in Fig. 3, the maximum sound power level for the rated winds occurs at around $f = 315$ Hz, which is chosen to show the results of the PE simulations. In Fig. 5, the distributions of RSPLD under six different conditions are depicted with the unit of color bar in dB. The six cases are different combinations of atmosphere and wake condition, as listed in Table 1. They all have flat ground treated as grasslands with flow resistivity $\sigma = 200$ kPa s m^{-2}.

It should be noted that the Rotor-rated wake (without tower or nacelle), shown in Fig. 2(a), is the input for the PE simulations, in this

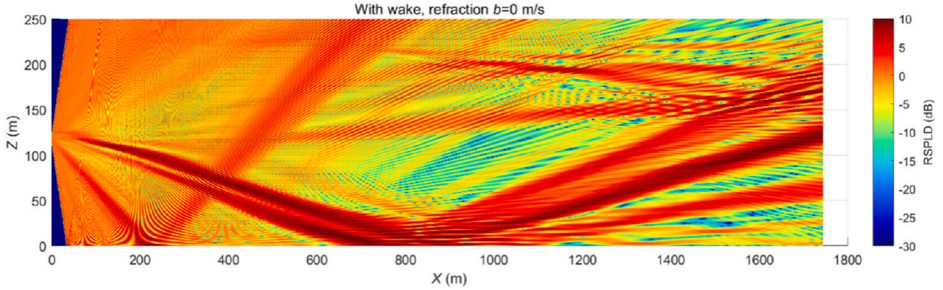

(a) CaseB

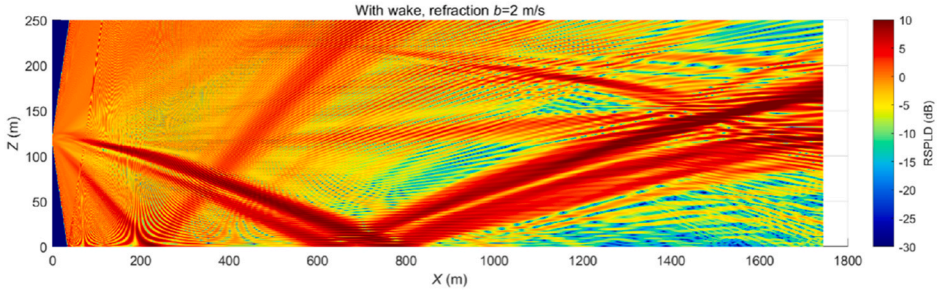

(b) CaseC

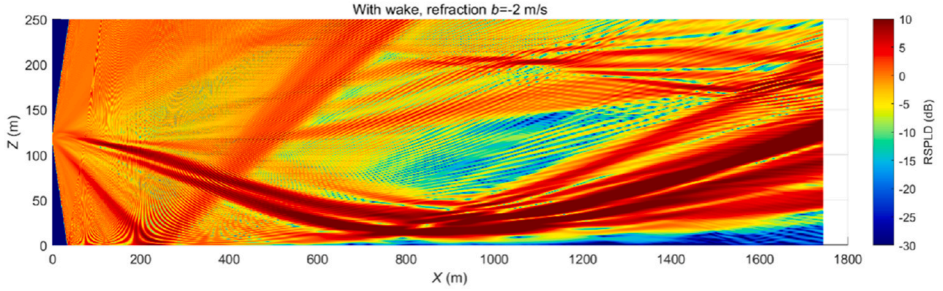

(c) CaseD

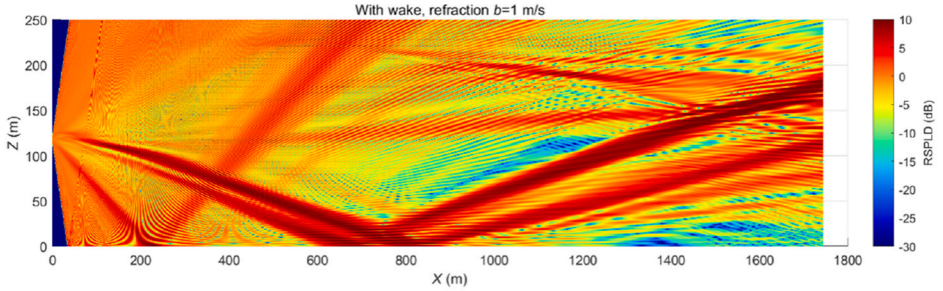

(d) CaseE

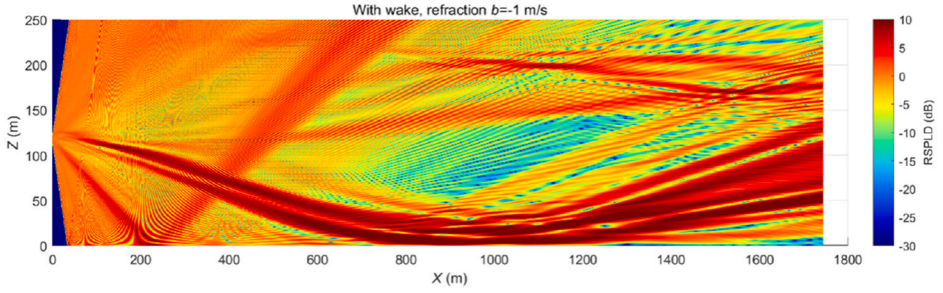

(e) CaseF

Fig. 8. The contour of RSPLD calculated by PE simulations at $f = 315$ Hz.

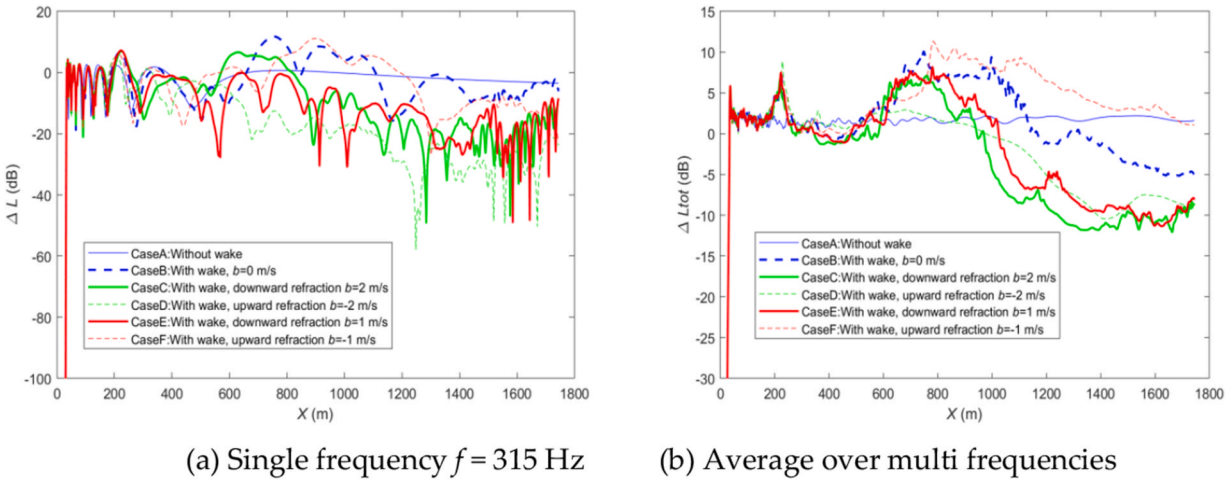

Fig. 9. The distribution of RSPLD along a horizontal line $Z = 2$ m.

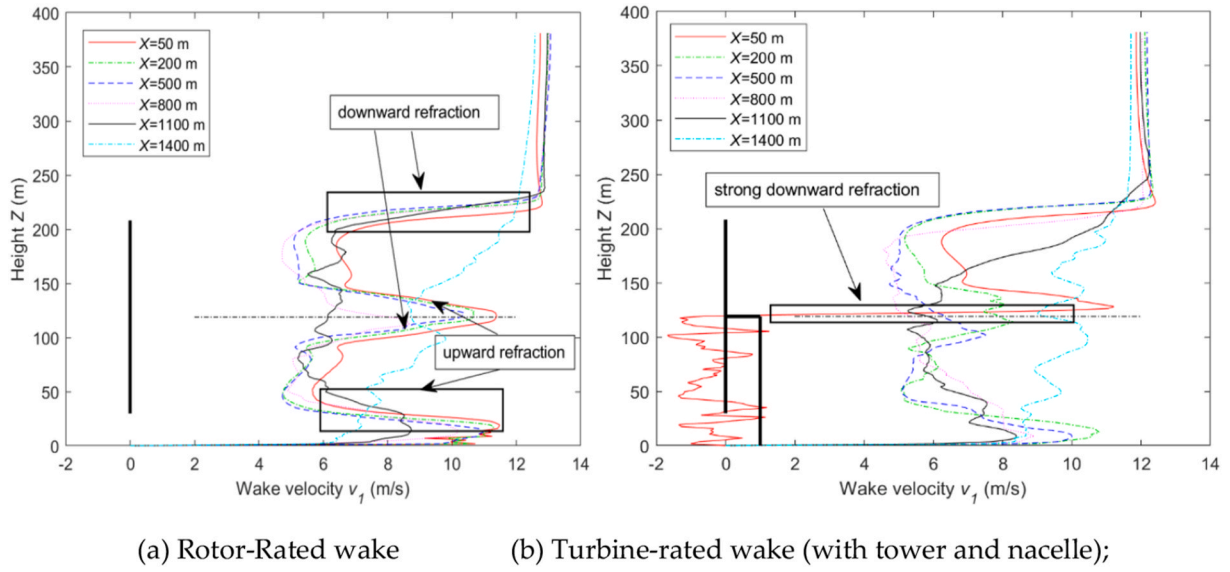

Fig. 10. Horizontal velocity v_1 along different vertical lines downstream.

section. In the next sections, the Turbine-Rated wake (with tower and nacelle), will be the input to the PE simulations. For CaseA in Fig. 5 (a), the propagation of the noise is mainly controlled by the direct sound wave and the reflected sound wave by the ground. For the other cases, the wake velocity from Fig. 2(a) is considered as the effective sound speed. As shown in Fig. 5(b–f), the RSPLD distribution is obviously more intricate than that of CaseA, which shows the effects of wake flow. As shown in Fig. 5 (b), the RSPLD contours of CaseB are almost symmetric with respect to the horizontal line dividing the hub height. For CaseD in Fig. 5(d), with a strong upward refraction b = −2 m/s, a quieter zone (X > 600 m) is observed near the ground. In the range of 1200 m < X < 1400 m, CaseF is obviously noisier than the other cases.

To investigate the impact of the propagated noise on humans, we focus on RSPLD (or ΔL) at Z = 2 m for different conditions, as represented in Fig. 6(a) for a single frequency of $f = 315$Hz and in Fig. 6(b) for multiple frequencies. If one wants to observe the total performance over multi frequencies, the variable $\Delta Ltot$ can be obtained through a logarithmic average over all frequencies:

$$\Delta Ltot = 10\log\left(\sum_{i=1}^{25}\frac{10^{\Delta L(fc_i)/10}}{25}\right), \tag{9}$$

here, we take all frequencies into account: a total of 25 center frequencies from $fc_1 = 20$ Hz to $fc_{25} = 5000$ Hz in the l/3-octave bands. As seen in Fig. 6(b), there is no obvious deviation from CaseA (without wake) and the other five cases in the range of X < 250 m. In the range 500 m < X < 800 m, where there might be residences, CaseA underestimates $\Delta Ltot$ than others except CaseC. The maximum underestimate is 0–5 dB. Additionally, in the range of 1100 m < X < 1600 m, CaseA predicts larger $\Delta Ltot$ than other cases (except CaseF).

The sound pressure level spectra $SPL(f)$ can be calculated using Eq. (7) at four receivers, which are compared in Fig. 7 by a 1/3-octave band. It should be noted that the third term of Eq. (7), the air absorption term $\alpha(f)D$, is calculated according to ISO 9613-1 [46], with a relative humidity of 80 % and temperature of 10 °C. The fourth term ΔL is calculated by the PE simulation. As the air absorption term is much larger than the other terms at f > 5000 Hz, the PE simulation is conducted at a maximum frequency of 5000 Hz. The label ISO in Fig. 7 is calculated according to the ISO-9613-2 standard [47] following

$$SPL_{ISO}(f) = SPWL\ (f) - 10\log_{10}(4\pi D^2) - \alpha(f)D - A_{gr}(f). \tag{10}$$

The first, second and third terms are the same as in Eq. (7) while the last term accounts for the ground effect as detailed in the ISO-9613-2,

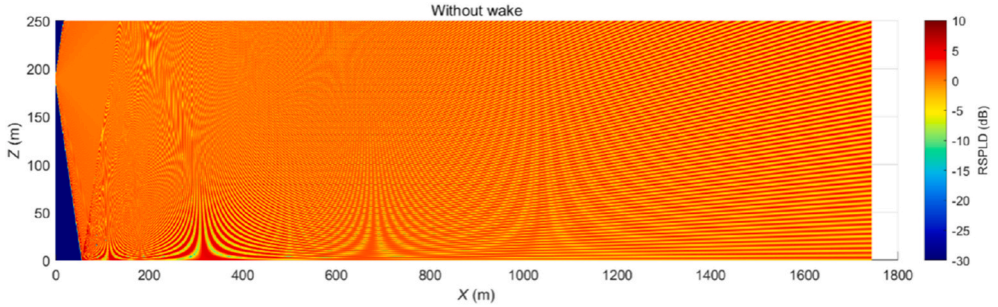

(a) CaseA

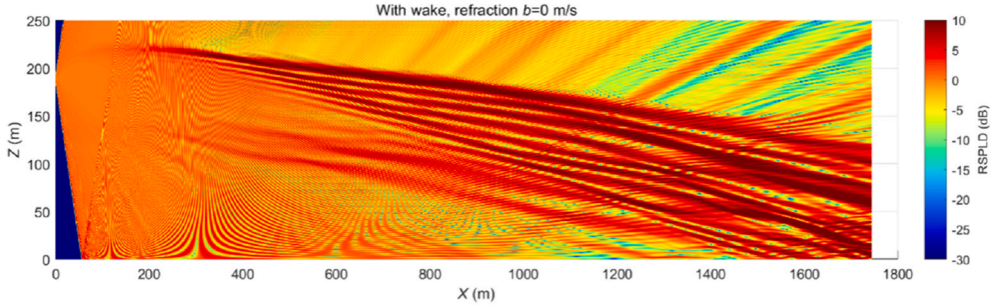

(b) CaseB

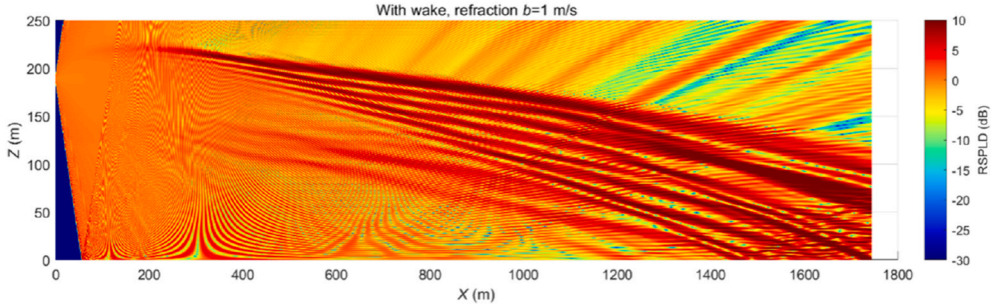

(c) CaseE

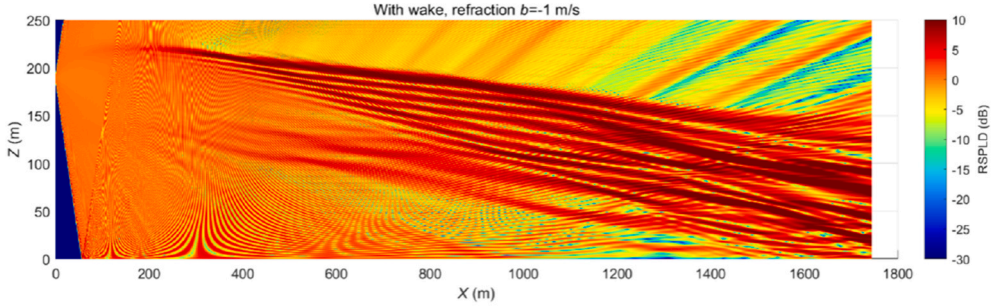

(d) CaseF

Fig. 11. The contour of RSPLD at $f = 315$ Hz, noise source at Z_{up}.

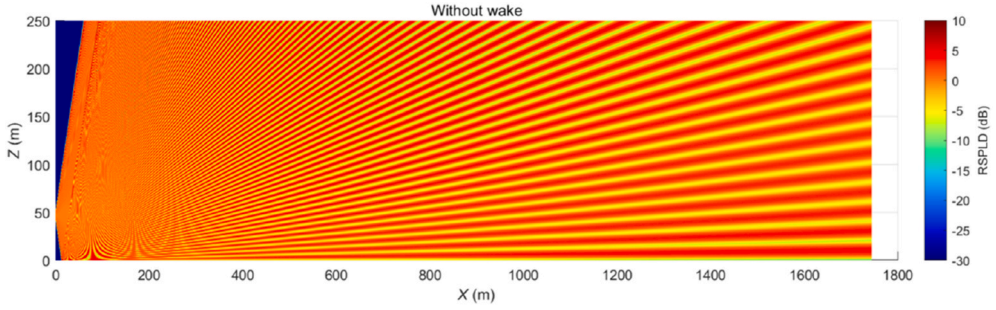

(a) CaseA

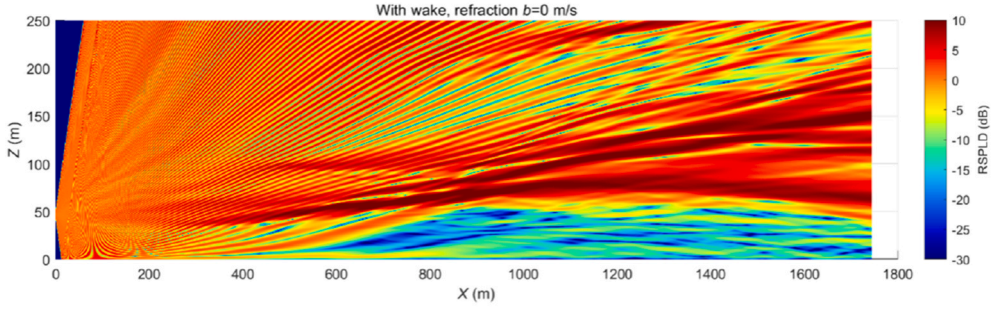

(b) CaseB

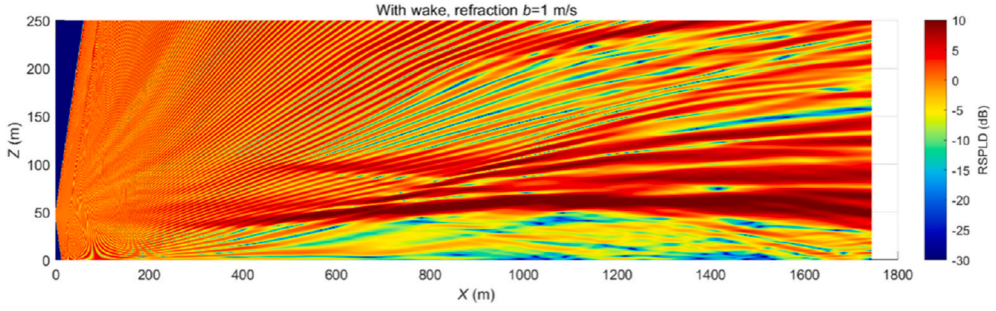

(c) CaseE

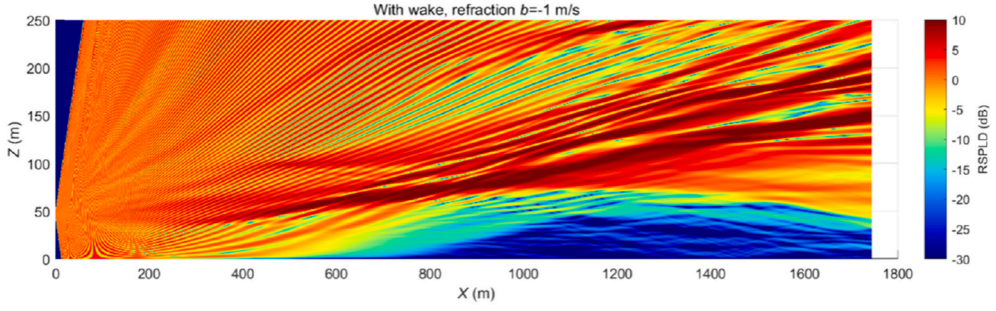

(d) CaseF

Fig. 12. The contour of RSPLD at $f = 315$ Hz, noise source at Z_{down}.

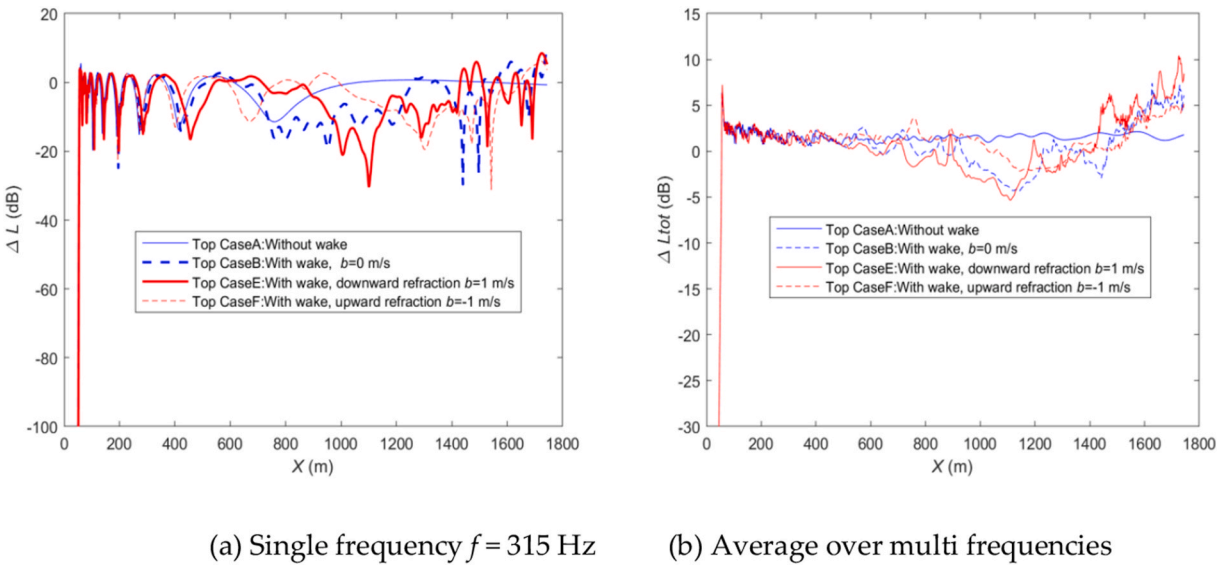

Fig. 13. The distribution of RSPLD along a horizontal line $Z = 2$ m, noise source at Z_{up}.

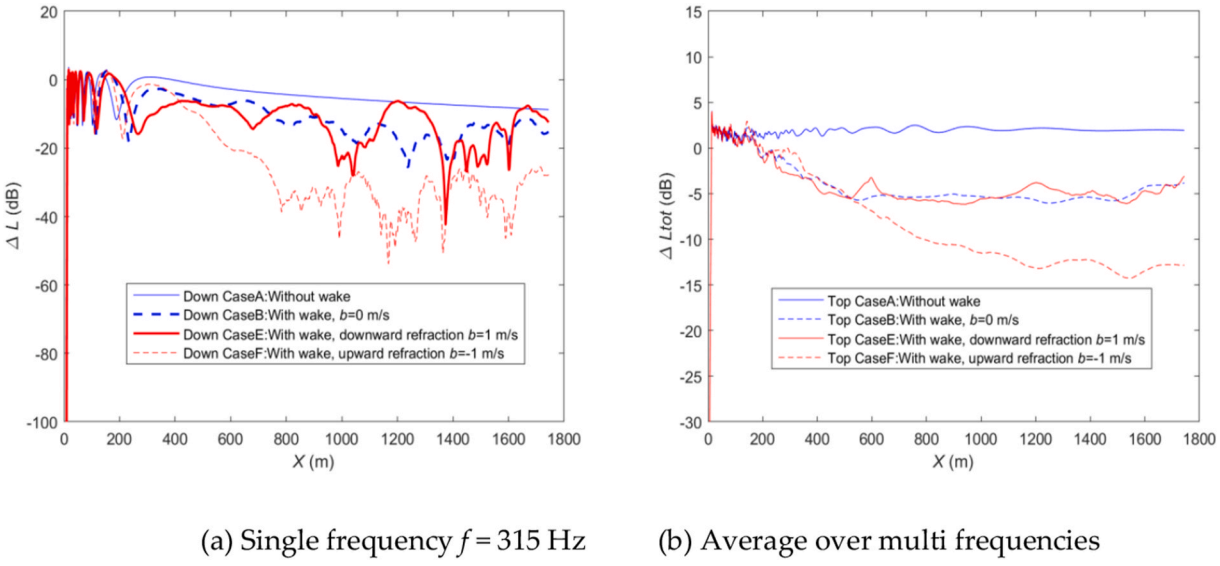

Fig. 14. The distribution of RSPLD along a horizontal line $Z = 2$ m, noise source at Z_{down}.

which considers ground reflections as

$$A_{gr}(f) = A_s(f) + A_r(f) + A_m(f). \tag{11}$$

Three attenuation factors can be defined: the source region attenuation $A_s(f)$ for the source region, the attenuation $A_r(f)$ for the receiver region, and the attenuation $A_m(f)$ for the middle region between the source and the receiver. These three factors are frequency-dependent and are calculated using the expressions provided in Ref. [47]. For the sake of brevity, these equations are not repeated here. However, they require the definition of ground factors as follows: $G_s = 1$ (to represent porous ground near source region), the ground factor $G_r = 0.6$ (to represent porous-hard mixed ground near receiver region) and the ground factor $G_m = 0.6$ (to represent porous-hard mixed ground in the middle region). First, the difference between the two black lines is caused by the air absorption term $\alpha(f)D$. It is obvious that this term is negligible for small frequencies, but it cannot be neglected for far locations, especially at high frequencies. Second, the spectrum $SPL(f)$ of CaseA to CaseF are much more complicated than the ISO-9613-2 method, which is the easiest way to calculate the propagation of noise in engineering usage. At receiver $X = 225$ m and receiver $X = 800$ m, the lines of CaseA to CaseF show a similar variation. With the further increase of the distance to $X = 1200$ m and $X = 1700$ m, the similarity between lines disappears and the low-frequency part has a greater contribution to the spectrum.

3.3. *Wind turbine noise propagation at the rated wind speed: effect of the tower and nacelle*

In this section, we include the tower and nacelle. Different from Section 3.2, the turbine-rated wake, shown in Fig. 2(b), is the input to the PE simulations. CaseA is not shown in Fig. 8, as it is the same as CaseA in Fig. 5. It is obvious that noisy red bands are seen in Fig. 8, which emit from the noise source and strike the ground at around X = 800 m. For CaseD in Fig. 8(d), with a strong upward refraction b = −2 m/s, a quieter zone ($X > 600$ m) is observed near the ground. The downward bending of the noisy red band does not 'touch' the ground, due to the strong upward refraction atmosphere. Weaker atmosphere refraction is considered in CaseE and CaseF, compared with that in

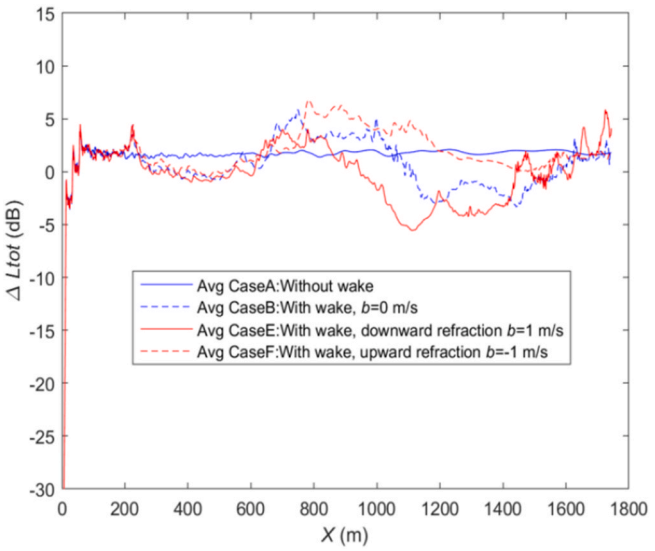

Fig. 15. The distribution of RSPLD along a horizontal line $Z = 2$ m, average over three heights and multi frequencies.

CaseC and CaseD. Unexpectedly, upward-refracted CaseF generates a longer noisy red band near the ground than its downward-refracted counterpart CaseE. The noisy band coincidentally 'floats' above the ground in a larger region 800 m $< X <$ 1200 m. If the upward refraction is stronger, CaseF will perform like CaseD, where the noisy red band is heavily curved upward so that it cannot even reach the ground. If the upward refraction is weaker, CaseF will perform like CaseB. In short, slightly upward refraction 'coincidentally' leads to the longest noisy red band near the ground.

The RSPLD at $Z = 2$ m are extracted from Fig. 8 and plotted in Fig. 9 for different cases. In the range $X > 150$ m of Fig. 9(a), the RSPLD of different cases start to deviate from each other. When $X > 700$ m, the RSPLD of CaseA starts to vary linearly with the propagation distance. This is because CaseA does not consider the effect of wind turbine wake. The other lines still have peaks and troughs, which are mainly due to the refraction effect captured by this PE solver. If we compare CaseC and its counterpart CaseD, the RSPLD of CaseD is generally lower than CaseC when $X > 500$ m. This observation aligns with our intuition that upward refraction results in lower noise levels at distant downstream positions. Setting $b = -2$ m/s in CaseD results in a lower effective sound speed at higher altitudes, shown in Fig. 4, which leads to up-bending or up-refracting of sound waves. Interestingly, this phenomenon is reversed between CaseE and CaseF, where CaseF (under upward refraction) has a higher noise level compared with its counterpart CaseE when $X > 500$ m. The higher noise level is in correspondence with Fig. 8(e) for its long-noisy band near the ground, which has already been discussed in detail above.

When considering all frequencies far downstream $X > 500$ m, all five cases except CaseA start to increase, then reach their maximum at different locations, and then start to decrease. Their differences increase abruptly when $X > 600$ m. These phenomena align with the different patterns of the noisy band in Fig. 8. The maxima location corresponds well with the striking ground location of the strong noisy band. In addition, CaseF obviously has a larger $\Delta Ltot$ compared to CaseE, which has been discussed above.

Until now, we have been trying to understand why there are noisy bands in Fig. 8 that do not appear in Fig. 5. Our initial hypothesis is that the difference arises from the distinct flow field inputs used in the parabolic equation (PE) solver. In the previous section, the Rotor-Rated wake was used as input to the PE solver. In contrast, the current section uses the Turbine-Rated wake, shown in Fig. 2(b), as the input. To further investigate this, we compare the two wakes by presenting the horizontal velocity component v_1 along several vertical lines downstream. In Fig. 10(a), the vertical distribution of the wake deficit is asymmetric with respect to the height of the hub $Z = 119$ m. In the height range 200 m $< Z <$ 230 m, corresponding to the boundary layer between the rotor wake and the free stream flow, the vertical gradient for the wake velocity v_1 is large, leading to a downward refraction of sound propagation. The height range 20 m $< Z <$ 50 m in Fig. 10(a), corresponding to the increased velocity region caused by the blocking effects of the rotor, also generates a large vertical gradient for the wake velocity v_1, which leads to upward refraction effects. Similarly, around the height of the hub $Z = 119$ m, there is also a vertical gradient of v_1, which leads to upward and downward refractions. These refractions split the contour in Fig. 5(b–f) into two symmetric parts with respect to the hub height after $X = 200$ m.

When considering the wind turbine wake with tower and nacelle shown in Fig. 10(b), the horizontal velocity profile v_1 is less symmetric compared to that in Fig. 10(a). This loss of symmetry in the wake leads to less symmetric RSPLD contour in Fig. 8, when compared to Fig. 5. Except for the refraction effects discussed for the Rotor-Rated wake, the Turbine-Rated wake has an additional large gradient of v_1 caused by tower wake at $X < 50$ m (right downstream of the tower). This

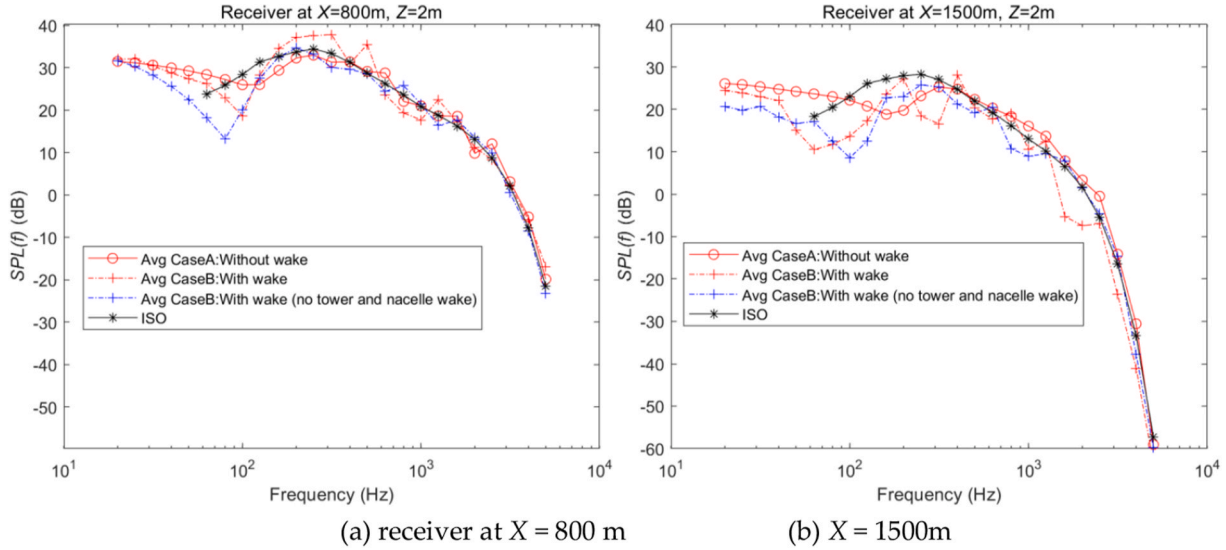

Fig. 16. Sound pressure level spectrum at two receivers at height $Z = 2$ m.

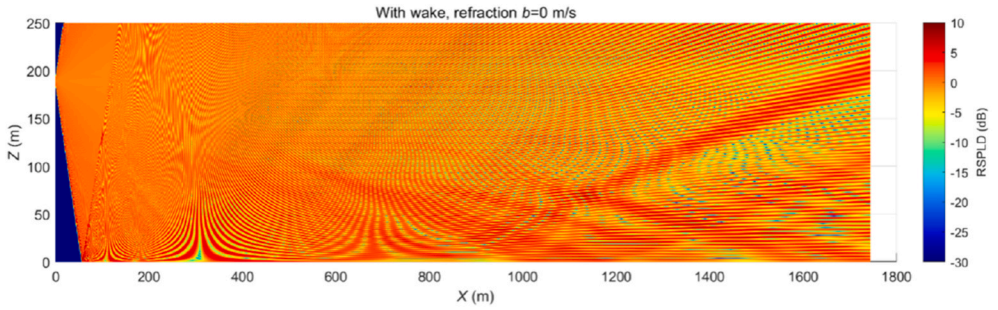

(a) Noise source located at the top of the rotor

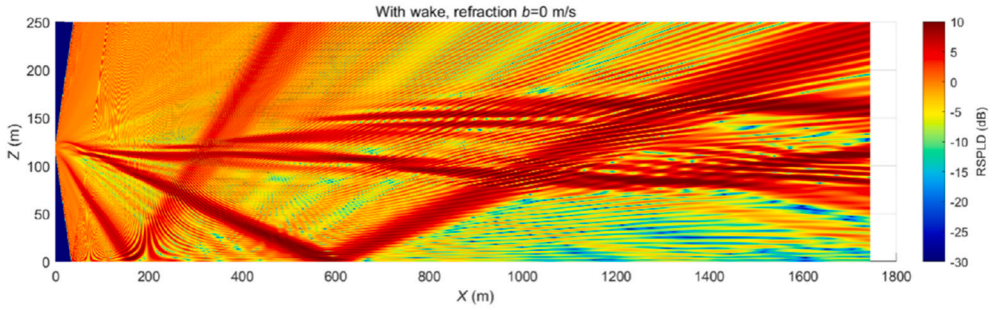

(b) Noise source located at the hub height

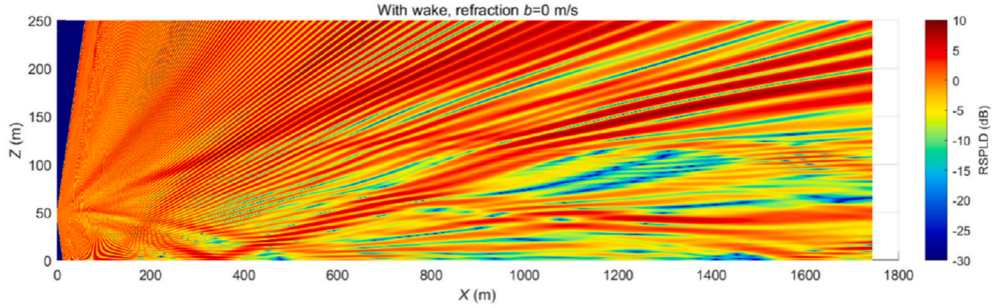

(c) Noise source located at the bottom of the rotor

Fig. 17. The RSPLD contour for CaseB (with wake, $b = 0$ m/s) at $f = 315$ Hz.

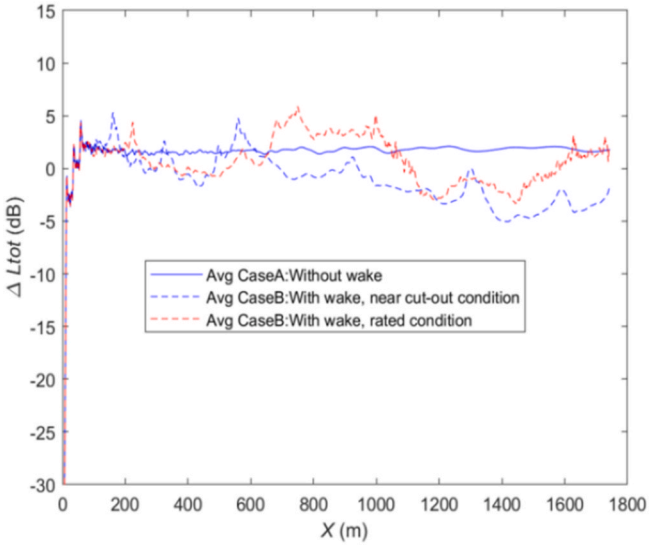

Fig. 18. The distribution of RSPLD along a horizontal line $Z = 2$ m.

contributes to downward refraction and results in a strong downward refraction after the tower, which makes Fig. 8 less symmetric compared with Fig. 5. There are two obvious noisy bands in Fig. 8(b), which reach the ground around $X = 200$ m and $X = 700$ m. The wake of the nacelle is similar to the wake of the hub, which should be symmetric with respect to the height line of the hub $Z = 119$ m. Therefore, the strong gradient of v_1 is mainly due to tower wake rather than nacelle wake. In other words, the strong downward refraction is mainly caused by the tower wake.

Consequently, the point noise source at the hub will be over-influenced by the strong gradient of v_1 from tower wake. This may lead to overpredicted downward refraction, because the noise source concentrate near the blade tip (i.e., typically at 80 % radius [48]). Therefore, in the next section, we investigate the propagation of sound with a noise source placed at different heights.

3.4. Wind turbine noise propagation at rated wind speed: effect of the noise source location

In the above two sections, the noise source is placed at the hub height. Here, the cases, listed in Table 1, are simulated again with the noise source placed at two other representative heights, $Z = Z_{up}$ and $Z = Z_{down}$. We use $Z_{up} = Z_{hub} + 0.8R$ and $Z_{down} = Z_{hub} - 0.8R$, as the sound power is concentrated near the tip of the blade [48]. Except for the height of the noise source, the other parameters are the same as used in

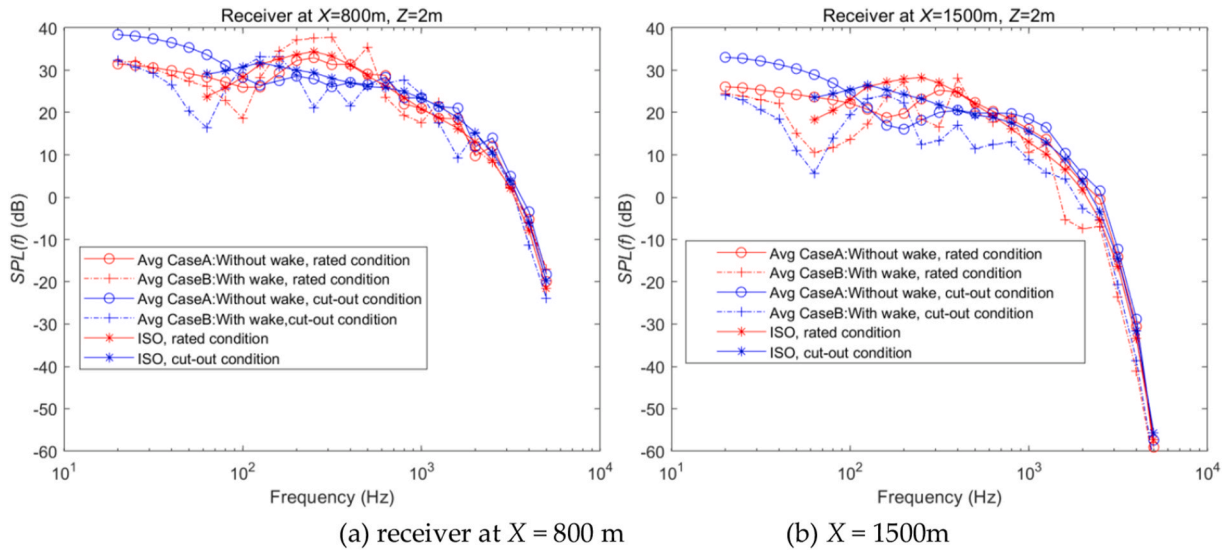

Fig. 19. Sound pressure level spectrum at two receivers at height $Z = 2$ m.

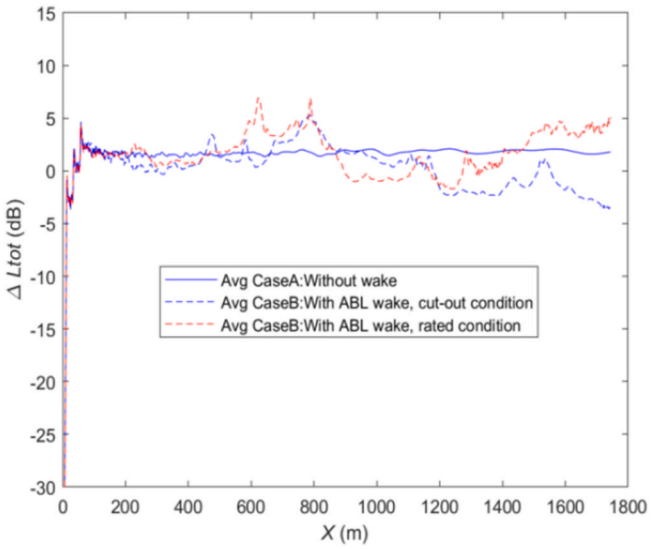

Fig. 20. The distribution of RSPLD along a horizontal line $Z = 2$ m.

Section 3.3, where the turbine-rated wake is the input to the PE simulation. The distributions of RSPLD are depicted in Figs. 11 and 12. Due to limited space for discussion, cases with strong atmospheric refraction (i.e., $b = \pm 2$ m/s) are not included in this section, as such conditions are rare in real-world scenarios.

Fig. 11(b–d) show that when the noise source is at the top, obvious noisy bands reach the ground around $X = 1600$ m. When the source moves to the bottom, as shown in Fig. 12(b–d), the RSPLD is lower for X > 600 m. It is found that the noise propagation patterns are different from those reported in the last section. The two obvious noisy bands, contacting the ground at around $X = 200$ m and $X = 800$ m, disappear in Figs. 11 and 12. To investigate the influence on humans, we extract the RSPLD (or ΔL) at $Z = 2$ m, which is plotted in Figs. 13 and 14. When the noise source is at the top, as shown in Fig. 13(b), CaseA predicts larger $\Delta Ltot$ than other cases in the range 800 m $< X <$ 1400 m. When $X >$ 1400 m, CaseA predict lower $\Delta Ltot$. When the noise source is down, as shown in Fig. 13(b), CaseA predicts a larger $\Delta Ltot$ compared with other cases (for the entire range).

To simplify further analyses, we use a logarithmic average, to obtain a height-averaged $\Delta L_{tot,}$ combing the three heights: Fig. 9(b), 13(b) and. 14(b). It should be stated that in Fig. 15, the label of 'Avg' means that the data are averaged over three heights of the noise source. CaseA (without wake input in the PE simulation) is found to be nearly a straight line, which gives a large underestimation in the range 700 m $< X <$ 900 m compared to other cases. In this range, Case A yields the lowest levels, and the cases with wake effects predict higher levels. Furthermore, CaseA tends to give an overprediction in the range of 1100 m $< X <$ 1600 m. The maximum underestimation and overprediction of CaseA, compared to other cases with wake, is around 5 dB, which is lower than in Fig. 9(b) with the noise source in the hub. Since these height-averaged results are only a simplification of the actual rotating noise source, they provide only an approximation of the average transient sound pressure level (SPL). As a result, key transient characteristics are lost, most notably amplitude modulation (AM), which plays an important role in human perception. AM originates from the periodic variation in the SPL during one full rotor revolution, caused by both the cyclic fluctuation in source strength and the rotating position of the noise source.

We choose two receivers from Fig. 15 to calculate the sound pressure level spectra *SPL(f),* using Eq. (7). Additionally, the ISO-9613-2 results by Eq. (10) is also plotted with noise source at hub height. One is located at $X = 800$ m, and the other is located at $X = 1500$ m. In Fig. 16, the label 'Avg' represents the height-averaged results. And the results from CaseB with rotor-only wake (not including tower and nacelle wake) is also plotted for comparison. At the receiver location $X = 800$ m, most of the deviation appears when $f < 1000$ Hz. The ISO-9613-2 method, Case A and CaseB without tower/nacelle wake significantly underestimate SPLs in the frequency range 200 Hz $< f <$ 500 Hz, where Case B considering whole wind turbine wake reaches approximately 40 dB—close to the lower threshold for wind turbine noise regulations near residences in many countries [49]. Such an underestimation could lead to an unsuitable allocation of wind turbines. Thus, to avoid wrong installation of wind turbines at 4.5 diameter upstream (800 m upstream) of the 10 MW wind turbine, it is advised to perform PE simulation with the whole wind turbine wake as input rather than only with the rotor wake. At $X = 1500$ m, the SPL drops below 30 dB, posing less concern, and the contribution of low-frequency components becomes more dominant.

3.5. *Wind turbine noise propagation at near cut-out wind speed*

In this section, we study the wind turbine operating at a near cut-out wind speed of 24 m/s, with Turbine-Cutout wake input into the PE simulations. The wake velocity shown in Fig. 2(c) will be the input of the PE simulations. When the noise source is at different heights, the RSPLD

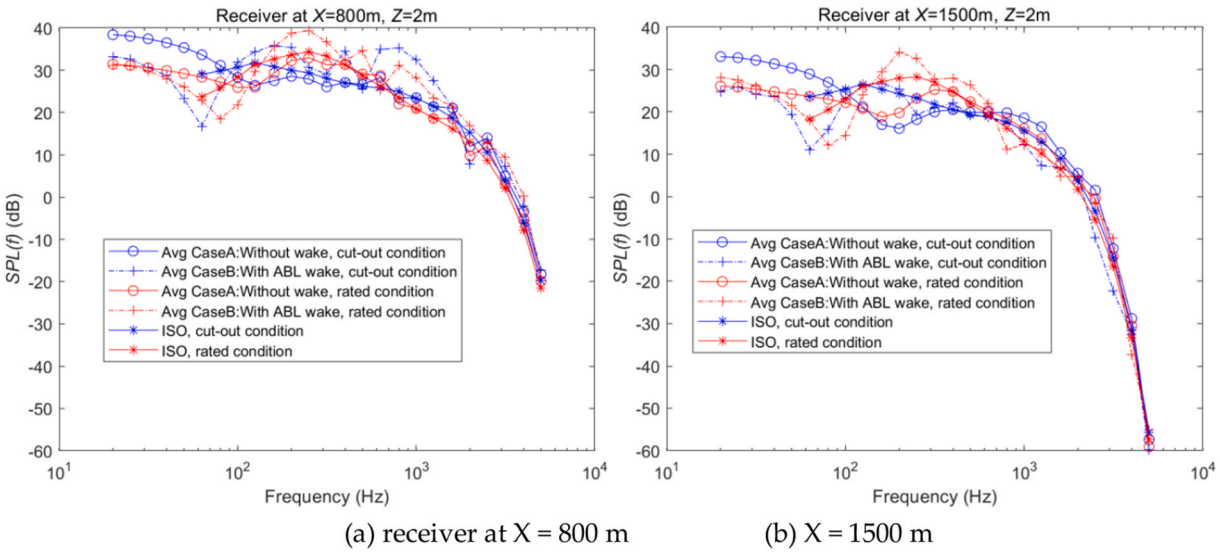

Fig. 21. Sound pressure level spectrum at two receivers at height $Z = 2$ m.

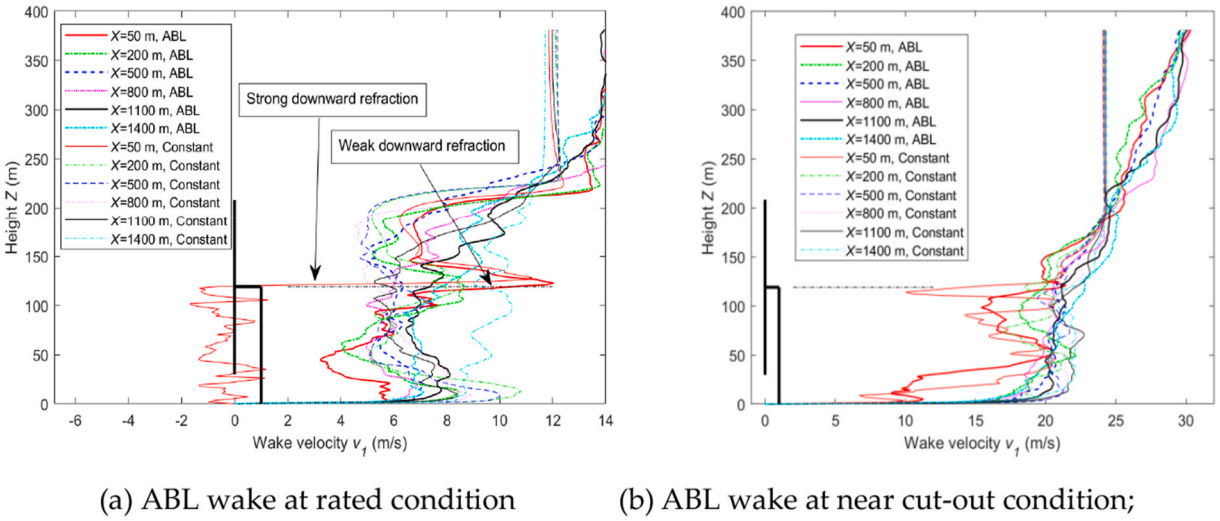

Fig. 22. Horizontal velocity v_1 along different vertical lines downstream.

contour of CaseB is shown in Fig. 17. When the noise source is at the top, Fig. 17(a) shows large differences with CaseB in Fig. 11(b), which is the rated wind speed and with noise source at the top. Fig. 17(a) resembles CaseA (without wake). Observing the flow field in Fig. 2(c) for the near cut-out condition, the velocity is nearly constant when Z > 150 m. This explains why there is less refraction at $Z > 150$ m compared to the rated condition. When the noise source is at the bottom, Fig. 17(c) does not generate low RSPLD regions, as in Fig. 12(b) at $X > 600$ m.

Using again use a logarithmic average, to obtain a height-averaged *ΔLtot*. Fig. 18 shows the noise at Z = 2 m, where the rated conditions (from Section 3.4) are also shown for comparison. Let us note that only the results are shown for b = 0 m/s are shown. We focus on the range 600 m < X < 1000 m, where the wind turbine wake introduces complexities in the SPL. In this range, the SPL is around 40 dB (as in Fig. 19), which is the lowest threshold of various noise regulations. Compared to the rated condition, the near cut-out condition has a lower SPL when X > 600 m.

For completeness, we again choose two receivers from Fig. 18 to calculate the sound pressure level spectra *SPL(f)*. Let us focus on the blue lines for near cut-out conditions, as the red lines for rated conditions are only for reference. The blue lines in Fig. 19 (a) have a similar trend to those in Fig. 19(b). Most deviations between blue lines happen in the low frequency range $f < 100$ Hz. This range contributes the most to the total SPL. The PE results without wake predict the largest SPL reaching 40 dB, which is the lower threshold of noise regulations. The PE with wake and ISO-9613-2 method predicts lower SPL. Compared to the rated condition, the near cut-out condition has a lower SPL in the middle frequency range around 300 Hz.

3.6. *Wind turbine noise propagation under a neutral atmospheric boundary layer*

Finally, in this last section we include a Neutral Atmospheric Boundary Layer (ABL), to assess the influence of incoming turbulence on wake development. In Sections 3.2 to 3.5, a continuous inflow velocity was used to isolate wake development from upstream disturbances. In this section, the wake resulting from a wind turbine simulation with a neutral ABL will be the input to the PE simulation. A detailed description of the neutral ABL can be found in Appendix B, where the flow field can also be found. We again study the logarithmic height-average *ΔLtot*. Fig. 20 shows the sound at $Z = 2$ m above the ground. Note that only the results under $b = 0$ m/s are shown. Comparing Fig. 20 with Fig. 18, they

are similar on the trend that the rated condition normally gives a higher SPL than the near-cut-out condition. The deviations between the red and blue lines in Fig. 20 are smaller than those in Fig. 18, which shows the effects of ABL.

We pay particular attention to the downstream distance of 600 m $<$ X $<$ 800 m, where the wind turbine wake complicates the SPL. Case B, which incorporates the ABL wake, consistently predicts the highest SPLs. As shown in Fig. 21(a), the SPL at this location is around 40 dB, near the lower threshold of some noise regulations. Under the rated condition, simulations using PE without wake effects, or relying solely on the ISO-9613-2 method, may underestimate SPL up to 5 dB and lead to inappropriate wind turbine sitting. When comparing Fig. 20 (using CFD with ABL inflow) with Fig. 18 (using CFD with constant inflow), the overall trends are similar, although the positions of peaks and valleys differ. The maximum $\Delta Ltot$ from the PE simulation with constant-inflow CFD is comparable to that with neutral ABL CFD. As illustrated in Fig. 22(a), the tower-induced downward refraction under ABL inflow is weaker than with constant inflow, which is more appropriate for modeling a hub-height point source. As discussed in Section 3.4 and illustrated in Fig. 16, PE simulations should use the full turbine wake, including the tower and nacelle, rather than the rotor wake alone. Feeding the CFD flow field (with ABL inflow) into the PE model yields a more realistic prediction of wind turbine noise propagation.

4. Conclusions

This study presents a comprehensive and systematic analysis of long-range sound propagation from a 10-MW wind turbine, integrating high-fidelity simulations with parabolic equation modeling to quantify the influence of tower-nacelle interactions, turbine operating conditions states, and atmospheric conditions. Key findings and implications are summarized as follows.

Tower and Nacelle Effects: The inclusion of tower and nacelle geometries in CFD simulations revealed asymmetric wake structures that significantly alter noise propagation paths. The downstream velocity gradients induced by the tower wake amplify downward refraction, increasing near-ground sound pressure levels (SPL) at 800 m compared to simulations that neglect these components. The height location of the source influences its propagation (for the same wake). While the proposed height-averaged SPL offers a simple way to account for rotor rotation, this simplification may limit the accuracy of the predicted phenomena. These effects require more detailed analysis and should be thoroughly investigated in future work.

Atmospheric conditions: Atmospheric conditions profoundly modulated propagation, under weak upward refraction (b = −1 m/s) extended noisy regions due to subtle wake-refraction interplay, highlighting the sensitivity of SPL to meteorological variability. Simulations using neutral ABL inflows emphasized the importance of realistic meteorological data, as ABL turbulence enhanced wake mixing and reduced refraction extremes from the tower wake.

Operational State Differences: The SPL difference between near cut-out and rated operation becomes noticeable beyond 600 m. Although the near cut-out condition produces lower SPL overall, it exhibits significantly higher levels in the 20–100 Hz band. This is partly because its noise-generation spectrum is dominated by low-frequency components and partly because low-frequency sound experiences less atmospheric attenuation.

Model Validation and Regulatory Implications: Under rated condition, simulations using PE without wake effects, or relying solely on the ISO-9613-2 method, may underestimate SPL by up to 5 dB at critical distances (around 500–1000 m) downstream, where residential areas could possibly be located. This emphasizes the limitations of simplified models. SPL underestimations could lead to unsuitable installation of wind turbines and should be treated with care. The PE framework, which can consider the whole wind turbine wakes and atmospheric profiles, provided high accuracy in capturing refraction and ground effects, advocating its adoption for regulatory compliance and wind farm planning.

Although this study focused on 2D propagation, future work should incorporate 3D PE models to resolve lateral wake dispersion and modulation effects of the amplitude. The point noise source omits directivity patterns and amplitude modulation associated with blade rotation. This approach may misrepresent the critical harmonic structures for annoyance assessments. In the future, the 2D PE simulation domain should follow blade rotation, or 3D PE should be used. The vertical temperature variation is simplified as a parabolic curve, which can be changed into real temperature profile test data. Experimental validation using field measurements under varied meteorological conditions would further refine the accuracy of the model. Low-frequency noise (<100 Hz) dominates beyond 1000 m downstream and propagates further with little air absorption. This phenomenon is beyond the scope of this article and warrants future study. While the 10 MW wind turbine is chosen as the object, the conclusion can be referenced for wind turbines of different size if we scale the contours with respect to the ratio of rotor size and tower height (e.g. downsize for 5 MW or upscale for 15 MW). Simulations for different wind turbines can be conducted in the future. Additionally, extending the framework to wind farm scales could optimize layout designs to minimize cumulative acoustic impact. By bridging high-order CFD and advanced acoustic propagation models, this work provides a robust methodology for addressing the environmental challenges of wind energy expansion, ensuring sustainable integration with residential communities.

CRediT authorship contribution statement

Zhenye Sun: Writing – review & editing, Writing – original draft, Visualization, Validation, Software, Methodology, Investigation, Funding acquisition, Formal analysis, Data curation, Conceptualization. **Weijun Zhu:** Validation, Software, Resources, Methodology, Investigation, Data curation. **Eduardo Jané:** Writing – review & editing, Writing – original draft, Visualization, Validation, Software, Investigation, Formal analysis, Data curation. **Xukun Wang:** Writing – original draft, Visualization, Investigation. **Wen Zhong Shen:** Software, Resources, Project administration, Funding acquisition. **Esteban Ferrer:** Writing – review & editing, Writing – original draft, Supervision, Software, Resources, Project administration, Methodology, Investigation, Funding acquisition, Conceptualization.

Data availability

The authors are committed to transparency and reproducibility in their research. Upon request, we are happy to provide the data used in this study. Please contact us directly for access to the datasets and any additional information needed to facilitate further investigation.

Declaration of competing interest

The authors declare that they have no known competing financial interests or personal relationships that could have appeared to influence the work reported in this paper.

Acknowledgements

This research has received funding from the European Union (ERC, Off-coustics, project number 101086075). However, the views and opinions expressed are those of the authors only and do not necessarily reflect those of the European Union or the European Research Council. Neither the European Union nor the granting authority can be held responsible for these.

This research was also supported by the China National Natural Science Foundation, No. 51905469, the Yangzhou Science and Technology Bureau (No. YZ2023247). Zhenye Sun wishes to express

acknowledgement to all who helped him to do research in Spain.

All authors gratefully acknowledge the Universidad Politécnica de Madrid (www.upm.es) for providing computing resources on Magerit Supercomputer and the computer resources at MareNostrum and the technical support provided by Barcelona Supercomputing Center (projects RES-IM-2024-1-0003 and RES-IM-2025-1-0011). Finally, the authors gratefully acknowledge the EuroHPC JU for the project EHPC-REG-2023R03-068 for providing computing resources of the HPC system Vega at the Institute of Information Science.

Appendix A. Validation of Mean-Flow Simulations

Large eddy simulations are conducted using Horses3D with actuator line methods. These high-order h/p solvers offer two distinct approaches to enhance numerical accuracy: h-refinement (increasing the number of mesh elements) and p-refinement (raising the polynomial order within each element), while traditional low-order methods (like finite-volume methods) can only improve accuracy through h-refinement. The p-refinement capability is particularly valuable, as higher-order polynomials achieve exponential error decay for smooth solutions, compared to the algebraic decay achieved by h-refinement in low-order methods. This makes the p-refinement generally more efficient in terms of degree-of-freedom utilization. Note that using a polynomial order P leads to a formal order of accuracy of P+1. That is, when we perform simulations with order 4, in fact, the order of convergence is 5 (or comparable to a finite-volume solver of order 5). In this work, we use P4 and P6, which correspond to orders 5 and 7. The base mesh used in all simulations has a total of 294492 hexahedral elements, and after automatic on-the-fly P-adaptation [50], results in a final number of 11339646, 10980780 and 7481019 degrees of freedom (DOFs) for the considered cases $V_{in} = 10$ m/s, 11.4 m/s and 24.0 m/s, respectively, with a maximum allowed polynomial order of 4. The decrease in the number of DOFs responds to the contraction of the rotor wake as the inflow wind speed increases, which is effectively detected by the P-adaptation algorithm in Horses3D. The additional validation case with $V_{in} = 10$ m/s and a maximum allowed polynomial order of 6, on the other hand, results in a final number of 28032208 DOFs. Fig. A-1 shows the instantaneous magnitude of the vorticity vector in the wake of the DTU 10-MW for the rated inflow wind speed $V_{in} = 11.4$ m/s and a maximum allowed polynomial order of 4, depicting how the simulation setup used captures the downstream propagation of the tip vortex and its dissipation further away from the rotor plane. The volumes in black represent the IBs of the nacelle and tower, downstream of which a shorter wake of higher vorticity magnitude can be observed.

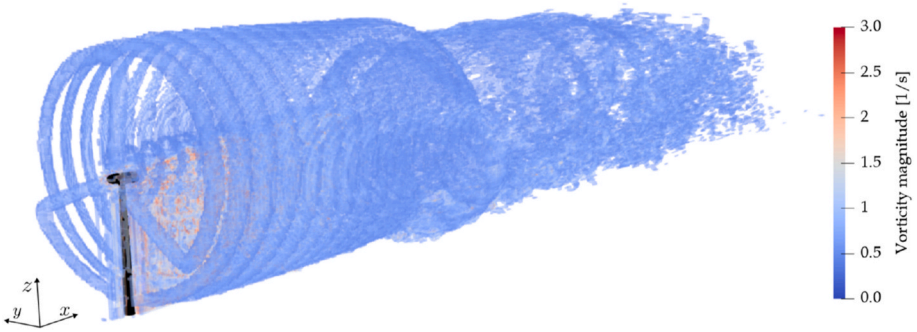

Fig. A-1. The magnitude of the vorticity vector in the wake of the DTU 10-MW simulation at the rated wind inflow speed Vin = 11.4 m/s. Volumes in black represent the nacelle and tower immersed boundaries.

The instantaneous LES wake velocity and the averaged flow fields are compared in Figs. A-2 and A-3. In Fig. A-2, the horizontal velocity is normalized by the V_{in} free stream inflow velocity using $1+(v_1 - V_{in})/V_{in}$. Note that the vertical and horizontal lines do not correspond to the mesh used in the CFD but are only grid axes showing positions in the domain. In Fig. A-3, the horizontal velocity along different downstream vertical lines is compared, where the wind turbine is sketched by a thick black line to show the correct rotor size. The tower position is shown to provide context (it is not in the right position). A black center line is drawn to show the height of the hub. By comparing Figs. A-2(a) and (b), the average wake is much smoother, not representing the smallest vortex structures. In Fig. A-3(a), the thick lines (averaged velocity) are close to their counterpart thin lines (instantaneous velocity). Comparing Figs. A-2(c) and (d), we can see the influence of the maximum polynomial orders (that is, the effective number of degrees of freedom per mesh element) on the averaged wake field under Vin = 10 m/s. In Fig. A-3(b), the influence of the maximum polynomial orders on wake along different vertical lines is compared. The differences between polynomial order 4 (P4, formal order 5) and 6 (P6, formal order 7) are small in the wake, so the P4 simulations are retained in what follows. Some differences can be seen after the tower X = 50 m, which is related to the IBM resolution used to include the shape of the tower, and far downstream (for X > 1200 m), which is related to the coarsening of the mesh in the CFD simulation far from the turbine. Despite this difference, the overall wake structure is well captured and does not depend on the polynomial used, showing mesh independence. A more detailed discussion of the choice of polynomial orders when using ALM in Horses3D can be found in Refs. [37, 51], where it has been shown that the use of high polynomials in coarse meshes is advantageous in terms of accuracy and relative cost. The current assessment of the velocity distributions along these vertical lines can help us understand the noise propagation phenomena discussed in Section 3.

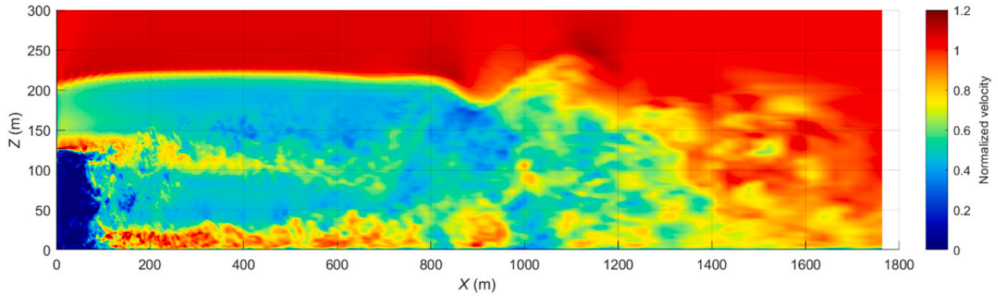

(a)instantaneous flow field under V_{in} = 11.4 m/s, maximum polynomial orders are 4.

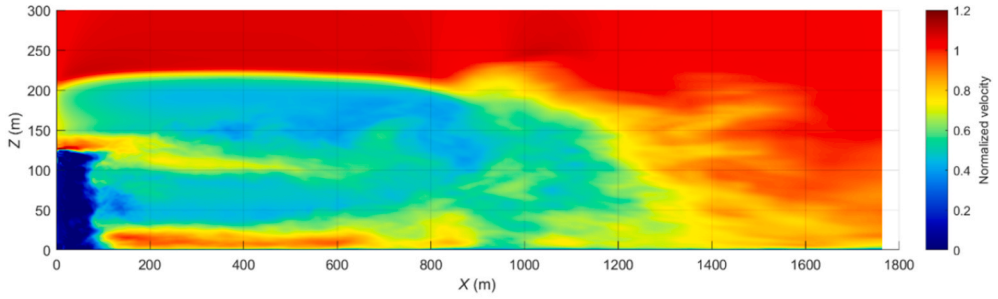

(b) Averaged flow field under V_{in} = 11.4 m/s, maximum polynomial orders is 4.

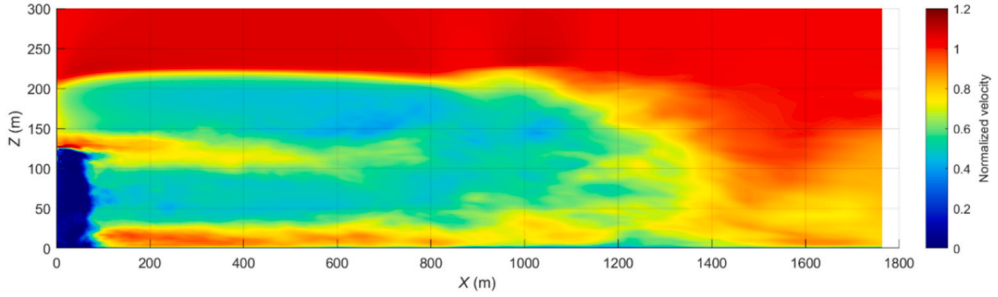

(c) Averaged flow field under V_{in} = 10 m/s, maximum polynomial orders are 4.

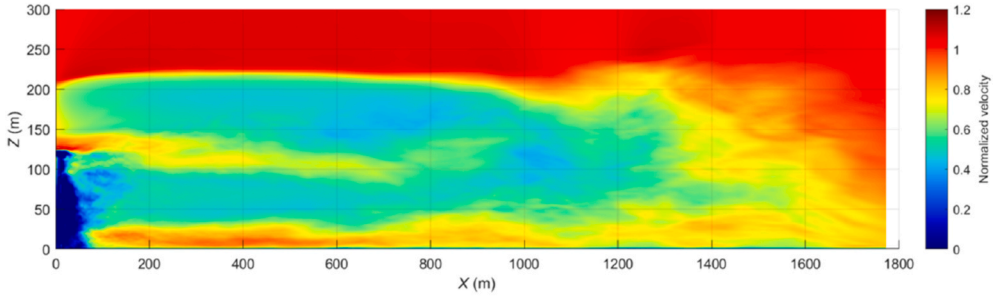

(d) Averaged flow field under V_{in} = 10 m/s, maximum polynomial orders are 6.

Fig. A-2. Horizontal velocity component downstream of the wind turbine from the CFD simulation. The underlying grid does not represent the CFD mesh and is only given for reference of the wake length.

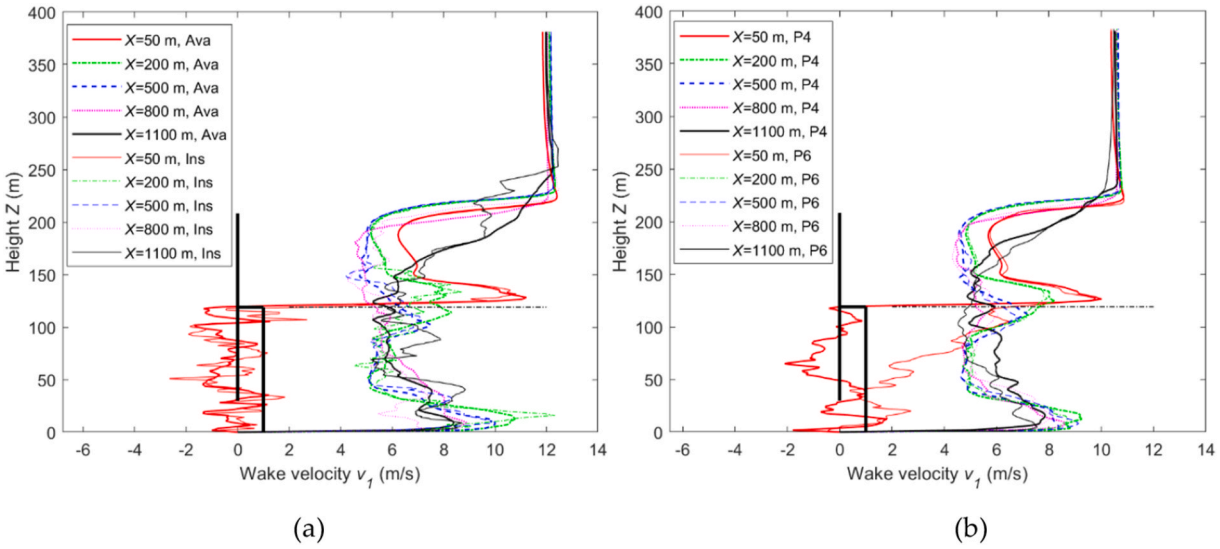

Fig. A-3. The horizontal velocity v_1 along different downstream vertical lines: (a) comparing the instantaneous and averaged wake under $V_{in} = 11.4$ m/s, Ava means averaged, Ins means Instantaneous; (b) averaged wake under $V_{in} = 10$ m/s wake, P4 and P6 mean the maximum polynomial orders 4 and 6. The tower position is not correctly placed in the figure and is included to provide context.

Additionally, Fig. A-4 shows the distribution of axial and tangential forces along the blade span for the $V_{in} = 10$ m/s case that results from the use of actuator lines in Horses3D with maximum polynomial orders of P4 and P6, compared to those of the equivalent blade-resolved CFD simulation presented in Ref. [42]. It can be noticed that, under these operating conditions, increasing the maximum allowed polynomial order only results in a relatively small improvement of the resulting force distributions when compared to those of the blade-resolved simulation, where the small differences observed near the tip and root of the blade can be attributed to the 3D flow effects that are not so accurately represented when using actuator lines.

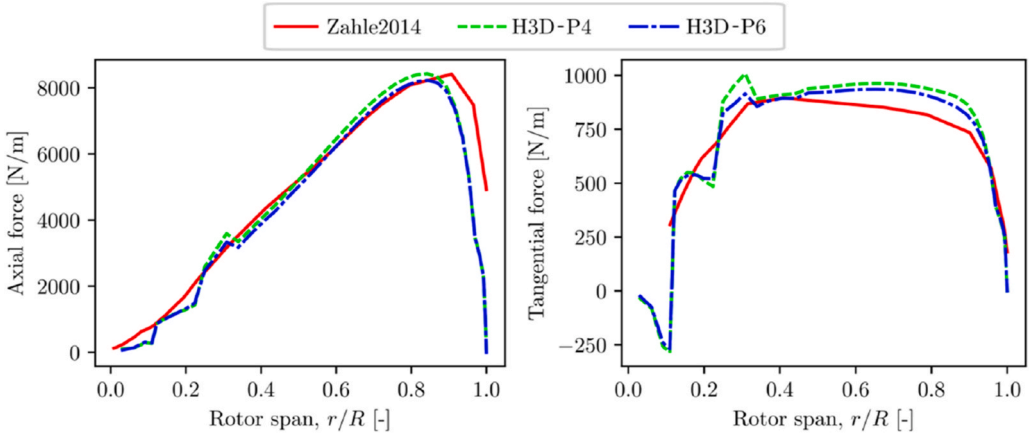

Fig. A-4. Comparison between the axial and tangential distributed forces along the blade span for the $V_{in} = 10$ m/s case presented by Zahle etc. [42] and those obtained from the actuator lines in the Horses3D simulations with a maximum allowed polynomial order of P4 (H3D-P4) and P6 (H3D-P6).

Appendix B. CFD Simulations with Neutral ABL and Precursor Simulations

The ABL inlet boundary conditions for wind speed, pressure, density, and temperature are mapped into the CFD solver at simulation runtime from precursor LES simulations, which is carried out using the NREL SOWFA toolbox [52]. The parameters taken in precursor simulations are based on those described in Ref. [45] for the neutral ABL case ($L_{MO} = \infty$), considering an aerodynamic roughness of $Z_0 = 0.05$ m, an approximate boundary layer height of 500 m, a grid resolution $\Delta_x \times \Delta_y \times \Delta_z$ of 16 × 10 × 5 m and a domain size $L_x \times L_y \times L_z$ of 3200 × 1600 × 1000 m. The potential temperature is constant through the neutral ABL, and the target boundary layer height is obtained by setting the central height of the initial strong capping layer at 550 m, with a width of 100 m and a potential temperature gradient of 0.003 K/m. The precursor simulation snapshots are obtained from the center of the domain with time-steps of 0.25 s and 0.1 s for the $u(z_{ref}) = 11.4$ m/s and 24.0 m/s cases, both corresponding to CFLs of slightly below 0.75. In this case, the reference height z_{ref} corresponds to the hub height of 119 m. Both precursor simulations have been run for 20000 s before starting the generation of snapshots to ensure a fully developed turbulent ABL. Finally, Fig. B-1 depicts the resulting time-averaged horizontal component of the velocity vector u_{mean}, and turbulent intensity TI_{mean} profiles with respect to height z for both ABLs. The dashed black lines represent the minimum and maximum rotor heights, and the dash-dot black lines represent the reference (hub) height. For completeness, we show in Fig. B-2 the instantaneous streamwise velocity component in the wake of the turbine obtained for rated and cut-out conditions filed, when using a neutral ABL.

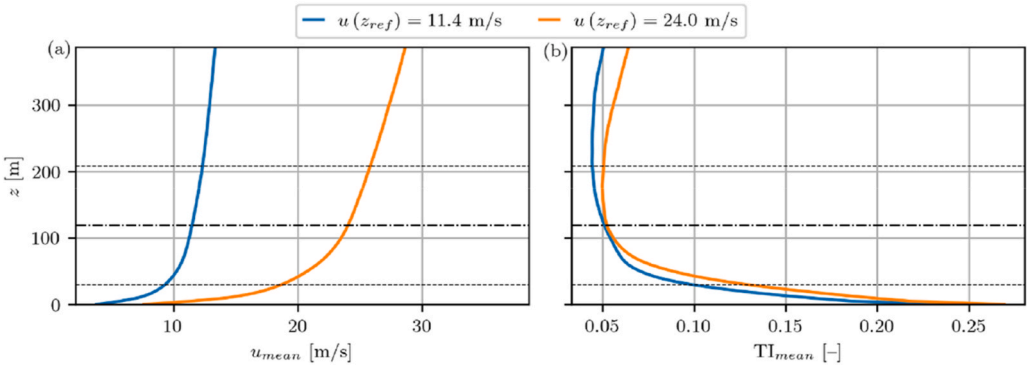

Fig. B-1ABL mean velocity profiles and turbulent intensity obtained from a precursor simulation and input in Horses3D. Both ABLs for rated and cut-out conditions are shown.

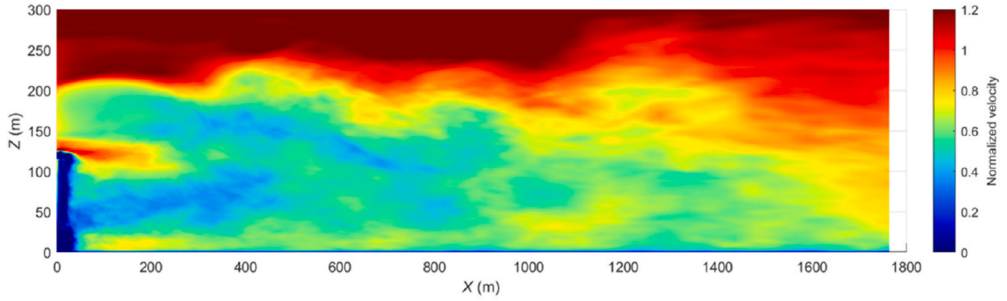

(a) Rotor-ABL Inflow-Rated: time-averaged flow field under $V_{in} = 11.4$ m/s

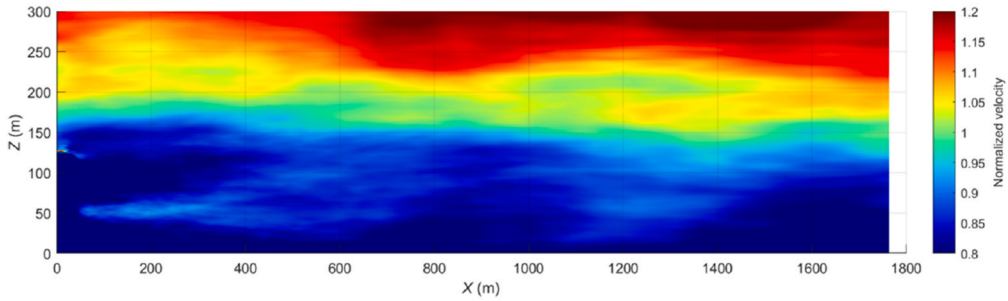

(b) Rotor-ABL Inflow-Near cut-out: time-averaged flow field under $V_{in} = 24.0$ m/s

Fig. B-2. Time-averaged flow fields (over three complete rotor revolutions) of the wind turbine wake under a neutral ABL.

References

[1] R.D. Sandberg, Compressible-flow DNS with application to airfoil noise, Flow Turbul. Combust. 95 (2–3) (Oct. 2015) 211–229, https://doi.org/10.1007/s10494-015-9617-1.

[2] R.D. Sandberg, N.D. Sandham, P.F. Joseph, Direct numerical simulations of trailing-edge noise generated by boundary-layer instabilities, J. Sound Vib. 304 (3–5) (Jul. 2007) 677–690, https://doi.org/10.1016/j.jsv.2007.03.011.

[3] J.C. Hardin, D.S. Pope, An acoustic/viscous splitting technique for computational aeroacoustics, Theor. Comput. Fluid Dynam. 6 (5) (Oct. 1994) 323–340, https://doi.org/10.1007/BF00311844.

[4] W.Z. Shen, J. Nørkær Sørensen, Aeroacoustic modeling of turbulent airfoil flows, AIAA J. 39 (6) (2001) 1057–1064, https://doi.org/10.2514/2.1446.

[5] W.Z. Shen, J.N. Sørensen, Aeroacoustic modelling of low-speed flows, Theor. Comput. Fluid Dynam. 13 (4) (Sep. 1999) 271–289, https://doi.org/10.1007/s001620050118.

[6] W.Z. Shen, J.A. Michelsen, J.N. Sørensen, A collocated grid finite volume method for aeroacoustic computations of low-speed flows, J. Comput. Phys. 196 (1) (May 2004) 348–366, https://doi.org/10.1016/j.jcp.2003.11.006.

[7] W.J. Zhu, W.Z. Shen, J.N. Sørensen, High-order numerical simulations of flow-induced noise, Int. J. Numer. Methods Fluid. 66 (1) (May 2011) 17–37, https://doi.org/10.1002/fld.2241.

[8] W.J. Zhu, N. Heilskov, W.Z. Shen, J.N. Sørensen, Modeling of aerodynamically generated noise from wind turbines, in: Journal of Solar Energy Engineering, Transactions of the ASME, Nov. 2005, pp. 517–528, https://doi.org/10.1115/1.2035700.

[9] Martin O.L. Hansen, Aerodynamics of Wind Turbines, third ed., Routledge, 2015.

[10] Z. Sun, J. Chen, W.Z. Shen, W.J. Zhu, Improved blade element momentum theory for wind turbine aerodynamic computations, Renew. Energy 96 (Oct. 2016) 824–831, https://doi.org/10.1016/j.renene.2016.05.035.

[11] T.F. Brooks, D.S. Pope, M.A. Marcolini, Airfoil self-noise and prediction [Online]. Available: https://ntrs.nasa.gov/citations/19890016302, Jul. 01, 1989. (Accessed 5 June 2025).

[12] M.C. Bérengier, B. Gauvreau, P. Blanc-Benon, D. Juvé, Outdoor sound propagation: a short review on analytical and numerical approaches, Acta Acustica united Acustica 89 (Feb. 2003) 980–991.

[13] O. Öhlund, C. Larsson, Meteorological effects on wind turbine sound propagation, Appl. Acoust. 89 (2015) 34–41, https://doi.org/10.1016/j.apacoust.2014.09.009.

[14] R. Raspet, et al., A fast-field program for sound propagation in a layered atmosphere above an impedance ground, J. Acoust. Soc. Am. 77 (2) (Feb. 1985) 345–352, https://doi.org/10.1121/1.391906.

[15] P. Boulanger, T. Waters-Fuller, K. Attenborough, K.M. Li, Models and measurements of sound propagation from a point source over mixed impedance ground, J. Acoust. Soc. Am. 102 (3) (Sep. 1997) 1432–1442, https://doi.org/10.1121/1.420101.

[16] S.N. Chandler-Wilde, D.C. Hothersall, Sound propagation above an inhomogeneous impedance plane, J. Sound Vib. 98 (4) (Feb. 1985) 475–491, https://doi.org/10.1016/0022-460X(85)90257-3.

[17] V.E. Ostashev, D.K. Wilson, Acoustics in Moving Inhomogeneous Media, second ed., 2015. London.
[18] E.M. Salomons, Computational Atmospheric Acoustics, first ed., 2001. Dordrecht.
[19] S.E. Keith, G.A. Daigle, M.R. Stinson, Wind turbine low frequency and infrasound propagation and sound pressure level calculations at dwellings, J. Acoust. Soc. Am. 144 (2) (Aug. 2018) 981–996, https://doi.org/10.1121/1.5051331.
[20] M.J. White, K.E. Gilbert, Application of the parabolic equation to the outdoor propagation of sound, Appl. Acoust. 27 (3) (Jan. 1989) 227–238, https://doi.org/10.1016/0003-682X(89)90062-5.
[21] M. West, K. Gilbert, R.A. Sack, A tutorial on the parabolic equation (PE) model used for long range sound propagation in the atmosphere, Appl. Acoust. 37 (1) (Jan. 1992) 31–49, https://doi.org/10.1016/0003-682X(92)90009-H.
[22] K.E. Gilbert, X. Di, A fast Green's function method for one-way sound propagation in the atmosphere, J. Acoust. Soc. Am. 94 (4) (Oct. 1993) 2343–2352, https://doi.org/10.1121/1.407454.
[23] S. Lee, D. Lee, S. Honhoff, Prediction of far-field wind turbine noise propagation with parabolic equation, J. Acoust. Soc. Am. 140 (2) (Aug. 2016) 767–778, https://doi.org/10.1121/1.4958996.
[24] D. Mascarenhas, B. Cotté, O. Doaré, Propagation effects in the synthesis of wind turbine aerodynamic noise, Acta Acustica 7 (2023) 23, https://doi.org/10.1051/aacus/2023018.
[25] Y. Tian, B. Cotte, Wind turbine noise modeling based on Amiet's theory: effects of wind shear and atmospheric turbulence, Acta Acustica united Acustica 102 (2016) 626–639.
[26] B. Cotté, Coupling of an aeroacoustic model and a parabolic equation code for long range wind turbine noise propagation, J. Sound Vib. 422 (May 2018) 343–357, https://doi.org/10.1016/j.jsv.2018.02.026.
[27] D. Heimann, Y. Käsler, G. Gross, The wake of a wind turbine and its influence on sound propagation, metz 20 (4) (Aug. 2011) 449–460, https://doi.org/10.1127/0941-2948/2011/0273.
[28] D. Heimann, A. Englberger, A. Schady, Sound propagation through the wake flow of a hilltop wind turbine— A numerical study, Wind Energy 21 (8) (Aug. 2018) 650–662, https://doi.org/10.1002/we.2185.
[29] D. Heimann, A. Englberger, 3D-simulation of sound propagation through the wake of a wind turbine: impact of the diurnal variability, Appl. Acoust. 141 (Dec. 2018) 393–402, https://doi.org/10.1016/j.apacoust.2018.06.005.
[30] E. Barlas, W.J. Zhu, W.Z. Shen, K.O. Dag, P. Moriarty, Consistent modelling of wind turbine noise propagation from source to receiver, J. Acoust. Soc. Am. 142 (5) (Nov. 2017) 3297–3310, https://doi.org/10.1121/1.5012747.
[31] E. Barlas, W.J. Zhu, W.Z. Shen, M. Kelly, S.J. Andersen, Effects of wind turbine wake on atmospheric sound propagation, Appl. Acoust. 122 (Jul. 2017) 51–61, https://doi.org/10.1016/j.apacoust.2017.02.010.
[32] E. Barlas, W.J. Zhu, W.Z. Shen, S.J. Andersen, Wind turbine noise propagation modelling: an unsteady approach, in: Journal of Physics: Conference Series, Institute of Physics Publishing, Oct. 2016, https://doi.org/10.1088/1742-6596/753/2/022003.
[33] J. Colas, A. Emmanuelli, D. Dragna, P. Blanc-Benon, B. Cotté, R.J.A.M. Stevens, Wind turbine sound propagation: Comparison of a linearized Euler equations model with parabolic equation methods, J. Acoust. Soc. Am. 154 (3) (Sep. 2023) 1413–1426, https://doi.org/10.1121/10.0020834.
[34] J. Colas, A. Emmanuelli, D. Dragna, P. Blanc-Benon, B. Cotté, R.J.A.M. Stevens, Impact of a two-dimensional steep hill on wind turbine noise propagation, Wind Energy Sci. 9 (10) (Oct. 2024) 1869–1884, https://doi.org/10.5194/wes-9-1869-2024.
[35] H. Bommidala, J. Colas, A. Emmanuelli, D. Dragna, C. Khodr, B. Cotté, R.J.A. M. Stevens, Three-dimensional effects of the wake on wind turbine sound propagation using parabolic equation, J. Sound Vib. 608 (2025) 119036.
[36] E. Ferrer, et al., A high-order discontinuous Galerkin solver for flow simulations and multi-physics applications, Comput. Phys. Commun. 287 (Jun) (2023), https://doi.org/10.1016/j.cpc.2023.108700.
[37] O.A. Marino, R. Sanz, S. Colombo, A. Sivaramakrishnan, E. Ferrer, Modelling wind turbines via actuator lines in high-order h/p solvers [Online]. Available: http://arxiv.org/abs/2406.09993, Jun. 2024.
[38] J. Kou, S. Joshi, A. Hurtado-de-Mendoza, K. Puri, C. Hirsch, E. Ferrer, Immersed boundary method for high-order flux reconstruction based on volume penalization, J. Comput. Phys. 448 (Jan) (2022), https://doi.org/10.1016/j.jcp.2021.110721.
[39] A.W. Vreman, An eddy-viscosity subgrid-scale model for turbulent shear flow: algebraic theory and applications, Phys. Fluids 16 (10) (2004) 3670–3681, https://doi.org/10.1063/1.1785131.
[40] V.E. Ostashev, D.K. Wilson, M.B. Muhlestein, Wave and extra-wide-angle parabolic equations for sound propagation in a moving atmosphere, J. Acoust. Soc. Am. 147 (6) (Jun. 2020) 3969–3984, https://doi.org/10.1121/10.0001397.
[41] M.E. Delany, E.N. Bazley, Acoustical properties of fibrous absorbent materials, Appl. Acoust. 3 (2) (Apr. 1970) 105–116, https://doi.org/10.1016/0003-682X(70)90031-9.
[42] F. Zahle, C. Bak, S. Guntur, N.N. Sørensen, N. Troldborg, Comprehensive aerodynamic analysis of a 10 MW wind turbine rotor using 3D CFD, in: 32nd ASME Wind Energy Symposium, 2014, https://doi.org/10.2514/6.2014-0359.
[43] C.M. Nyborg, K. Bolin, I. Karasalo, A. Fischer, An inter-model comparison of parabolic equation methods for sound propagation from wind turbines, J. Acoust. Soc. Am. 154 (2) (Aug. 2023) 1299–1314, https://doi.org/10.1121/10.0020562.
[44] T. Evans, J. Cooper, Effects of different meteorological conditions on wind turbine noise, in: Proceedings of Acoustics 2013, Australian Acoustical Society, Nov. 2013, pp. 1–9.
[45] M. Abkar, F. Porté-Agel, Influence of atmospheric stability on wind-turbine wakes: a large-eddy simulation study, Phys. Fluids 27 (3) (Mar. 2015) 035104, https://doi.org/10.1063/1.4913695.
[46] International Organization for Standardization, ISO 9613-1, acoustics-attenuation of sound during propagation outdoors: part 1: calculation of the absorption of sound by the atmosphere [Online]. Available: https://www.iso.org/standard/17426.html, 1993.
[47] International Organization for Standardization, ISO 9613-2, acoustics-attenuation of sound during propagation outdoors: part 2: general method of calculation [Online]. Available: https://www.iso.org/standard/20649.html, 1996.
[48] S. Oerlemans, P. Sijtsma, B. Méndez López, Location and quantification of noise sources on a wind turbine, J. Sound Vib. 299 (4–5) (Feb. 2007) 869–883, https://doi.org/10.1016/j.jsv.2006.07.032.
[49] Dr G. Arivukkodi, Dr S. Kanmani, Acoustic noise emission in wind turbine: an overview, Int. J. Res. Appl. Sci. Eng. Technol. 10 (9) (Sep. 2022) 1686–1697, https://doi.org/10.22214/ijraset.2022.46896.
[50] D. Huergo, M. de Frutos, E. Jané, O.A. Marino, G. Rubio, E. Ferrer, Reinforcement learning for anisotropic p-adaptation and error estimation in high-order solvers [Online]. Available: http://arxiv.org/abs/2407.19000, Jul. 2024.
[51] H. Kessasra, M. Cordero-Gracia, M. Gómez, E. Valero, G. Rubio, E. Ferrer, A comparison of h- and p-refinement to capture wind turbine wakes [Online]. Available: http://arxiv.org/abs/2409.16901, Sep. 2024.
[52] NREL/SOWFA, Roff, National Renewable Energy Laboratory, May 05, 2025 [Online]. Available: https://github.com/NREL/SOWFA. (Accessed 9 May 2025).